The Astrophysical Journal, 905:42 (32pp), 2020 December 10 https://doi.org/10.3847/1538-4357/abc332

Searching for Nuclear Obscuration in the Infrared Spectra of Nearby FR I Radio Galaxies

R. C. Gleisinger[1], C. P. O'Dea[2], J. F. Gallimore[3], S. Wykes[2], and S. A. Baum[4]
[1] Department of Physics and Astronomy, University of Victoria, Victoria, BC V8P 5C2, Canada
[2] Department of Physics and Astronomy, University of Manitoba, Winnipeg, MB R3T 2N2, Canada
[3] Department of Physics and Astronomy, Bucknell University, Lewisburg, PA 17837, USA
[4] Faculty of Science, University of Manitoba, Winnipeg, MB R3T 2N2, Canada
Received 2019 July 26; revised 2020 September 21; accepted 2020 October 12; published 2020 December 10

Abstract

How do active galactic nuclei with low optical luminosities produce powerful radio emission? Recent studies of active galactic nuclei with moderate radio and low optical luminosities (Fanaroff & Riley class I, FR I) searching for broad nuclear emission lines in polarized light, as predicted by some active galactic nucleus unification models, have found heterogeneous results. These models typically consist of a central engine surrounded by a torus of discrete dusty clouds. These clouds would absorb and scatter optical emission, blocking broad nuclear emission lines, and reradiate in mid-infrared. Some scattered broad-line emission may be observable, depending on geometry, which would be polarized. We present a wide-band infrared spectroscopic analysis of 10 nearby FR I radio galaxies to determine whether there is significant emission from a dusty obscuring structure. We used Markov Chain Monte Carlo algorithms to decompose Spitzer/IRS spectra of our sample. We constrained the wide-band behavior of our models with photometry from the Two Micron All Sky Survey, Spitzer/IRAC, Spitzer/MIPS, and Herschel/SPIRE. We find that one galaxy is best fit by a clumpy torus and three others show some thermal mid-infrared component. This suggests that in those three there is likely some obscuring dust structure that is inconsistent with our torus models and there must be some source of photons heating the dust. We conclude that 40% of our FR I radio galaxies show evidence of obscuring dusty material, possibly some other form of hidden broad-line nucleus, but only 10% favor the clumpy torus model specifically.

Unified Astronomy Thesaurus concepts: Spectroscopy (1558); Low-luminosity active galactic nuclei (2033); Infrared astronomy (786); Markov chain Monte Carlo (1889)

1. Introduction

1.1. AGN Unification

Active galactic nuclei (AGNs) show an array of different spectra that are usually grouped into broad categories based on their radio luminosities, bolometric luminosities, and the presence or absence of broad optical emission lines. AGN unification models attempt to explain many of these different classes with a single type of object that differs in only a few parameters. Its particular focus is to explain the presence or absence of optical broad lines in objects that are otherwise similar (e.g., similar radio and X-ray profiles). These models consist of a central engine and some anisotropic distribution of gas and dust that scatters or absorbs light from the central engine. The central engine is matter accreting onto a supermassive black hole. Our description of this model follows the one by Antonucci (1993). For further reading see Antonucci (2012), Tadhunter (2016), and Padovani et al. (2017).

In these models, material accreting onto the central supermassive black hole forms an optically thick but geometrically thin accretion disk that is obscured from some lines of sight by an optically thick, warm (~200–1000 K) mass of dusty material with a roughly toroidal geometry. This torus would absorb optical emission from the central engine and reradiate that energy in the infrared. Pier & Krolik (1992, 1993) modeled the torus as a smooth continuous cloud of variable density due to computing constraints, but they believed it to be composed of discrete clouds ("clumpy"). The alternative to a torus is that the central engine is intrinsically dim in the optical rather than obscured, resulting in a lower mid-IR (MIR) luminosity where warm obscuring dust would radiate. Smooth torus models require fine tuning in order to match the suppressed low equivalent width 10 μm silicate features observed in infrared spectra (Granato & Danese 1994; Granato et al. 1997).

Rowan-Robinson (1995) claimed that clumpy torus models can adequately explain silicate feature suppression observed in Seyfert 1 galaxies but, just like Pier & Krolik (1992), lacked a fully 3D radiative transfer code to fully explore it. Nenkova et al. (2002, 2008a, 2008b) formalized the clumpy torus model we consider in our decompositions in Section 5. This model describes an obscuring torus as being composed of small, discrete, optically thick clouds. The inner radius of the torus is determined by the sublimation radius R_d for the component dust grains i.e., the minimum distance from the central engine at which a grain can survive. This sharp boundary is an approximation since larger dust grains can survive significantly closer to the central engine than the inner edge of the main torus (Pier & Krolik 1993; Schartmann et al. 2005). The remaining parameters that Nenkova et al. (2008a, 2008b) include in their torus model are the optical depth of a single torus clump at 550 nm, τ_V (assumed to be the same for all clumps), the mean number of clouds along a radial equatorial line, N_0, the radial extent of the torus in units of the dust sublimation, Y, the inclination of the torus with respect to the line of sight, i (defined such that 0° is pole-on), the angular scale height of the torus (effectively the standard deviation of the normally distributed clumps around the equator), σ, and the power-law index of the radial distribution of clumps, q. From these parameters they show how to calculate the half-opening

angle of the torus, the torus height-to-radius ratio $H/R = \tan(\sigma)$, and the photon escape probability.

There are alternatives to the unification model in which the central engines of low-luminosity sources intrinsically differ from those of high-luminosity sources. These are largely beyond the scope of this paper, but they often involve an advection-dominated accretion flow (ADAF), in which a supermassive black hole is accreting at below 1% of the Eddington rate and the infalling material does not radiate much of its energy away (see, e.g., Narayan et al. 1998; Best & Heckman 2012).

1.2. Existing Evidence in FR I Radio Galaxies

Fanaroff & Riley class I (FR I; Fanaroff & Riley 1974) radio galaxies are low-luminosity radio galaxies with subrelativistic jets that are brightest near their cores. FR I radio galaxies typically do not show significant broad optical line emission, though there are exceptions such as 3C 120 (French & Miller 1980; Leipski et al. 2009; Torrealba et al. 2012). The question of how FR I radio galaxies fit into AGN models can be reduced to two separate but related parts. These are the nature of the accretion structure that powers the radio jet and the structure of any obscuring material. These are related because if FR I galaxies are powered by an accretion structure with a high intrinsic optical luminosity such as a Keplerian thin accretion disk, then the central engine must be obscured in order to match observations.

Haas et al. (2004) analyzed 5–200 μm photometry from the photometer on the Infrared Space Observatory, ISOPHOT, of 75 objects in the Revised Third Cambridge Catalog of radio galaxies and quasars (Laing et al. 1983), including five FR I sources (of which three overlap with our sample). They clearly detect a thermal component in the FR I galaxies despite the lower sensitivity compared to Spitzer (Kessler et al. 1996), but it was too cold to be consistent with the unification models we are considering. Chiaberge et al. (1999) detected the central core component in 85% of Hubble Space Telescope (HST) observations of FR I radio galaxies and so put an upper limit on the covering fraction of any obscuring torus with the caveat that the base of an optical jet may appear as an alternate source of optical continuum emission. Whysong & Antonucci (2004) found that the MIR core component of M87 is dominated by synchrotron emission from the base of its relativistic jet, and Perlman et al. (2007) put further limits on a a warm obscuring torus in M87. These findings effectively rule out the possibility of a significant amount of obscuring warm dust. Van der Wolk et al. (2010) found no evidence for warm dust tori in any of the eight FR I sources in their observations from the Very Large Telescope's Imager and Spectrometer for mid-Infrared. Note that one of the FR I sources in the van der Wolk et al. (2010) sample is 3C 270, which is also in our sample. In HST images of the optical nuclei of a sample of 54 FR I and 55 FR II radio galaxies at $z < 0.3$, Kharb & Shastri (2004) found that the optical emission in these sources is primarily nonthermal emission from a relativistic jet. Their fits also showed no significant improvement from including a thermal accretion disk in the FR II population as a whole but found some improvement from including a disk component in broad-line-emitting FR II galaxies. They claim that this is supported by the presence of a "big blue bump," which they attribute to an accretion disk. Kharb & Shastri (2004) additionally found that the luminosities of the optical nuclei in FR I radio galaxies show strong dependence on the radio core prominence R_c, which is a common statistical indicator of orientation, and from this they conclude that their results are consistent with the lack of a torus in FR I radio galaxies. In a study conceptually similar to ours, González-Martín et al. (2015) searched for AGN obscuration in Spitzer/IRS (see Section 3) spectra and Chandra photometry of a sample of low-ionization nuclear emission region AGNs. The dusty torus present in brighter sources disappeared below bolometric luminosities $L_{\rm bol} \simeq 10^{42}$ erg s^{-1}, consistent with Elitzur & Shlosman (2006) and that the MIR spectra of such sources are dominated by host, jet, and/or ADAF emission.

Leipski et al. (2009) found a Spitzer/IRS band thermal excess attributed to warm nuclear dust emission in 4 of the 15 galaxies with detected optical compact cores in their sample of 25 FR I radio galaxies. Six of our 10 sources—3C 31, 3C 66B, NGC 3862, 3C 270, M84, and M87—overlap with their sample. Of those, they only found thermal MIR excess in the nuclei of 3C 270 and M84, which they tentatively attribute to an obscuring torus and starburst activity, respectively. However, Wu & Cao (2006) give a star formation rate (SFR) estimate of $0.20\,M_\odot$ yr^{-1} for M84, which is inconsistent with a starburst. They also found an MIR excess in 3C 66B, which they attribute to nonthermal emission. Leipski et al. (2009) also found a very low ratio between the 7.7 μm and 11.3 μm PAH lines, which is not typical for starburst galaxies.

In contrast, Bianchi et al. (2019) found red and blue wings on line emission in NGC 3147 consistent with the profile of a mildly relativistic thin Keplerian accretion disk. NGC 3147 is an unobscured AGN with an accretion rate far below the Eddington rate ($\sim 10^{-4} L/L_{\rm Edd}$) that lacks a broad-line region. The detection of an accretion disk in such an object suggests the possibility that extremely low accretion rates can still support thin accretion disks.

Overall, recent studies favor the two-mode models in which some, but not all, FR I radio galaxies have some sort of obscuring material around their central engines. The remainder are believed to have central engines that are too dim in IR and optical to distinguish from their host galaxies. These dim central engines would still produce jets that may appear in the IR as a synchrotron spectrum. This is likely due to environmental factors such as the source of the accreting material. For example, cold source material may be more likely to form a disk, while hot material may be more likely to form an ADAF. The structure of this obscuring material is, however, not necessarily a torus like that described by Nenkova et al. (2002, 2008a, 2008b).

1.3. Overview

To determine what powers the central engine in FR I radio galaxies and how they fit into the broader picture of AGNs, we search for the signature of warm obscuring dust in the infrared spectra of 10 nearby FR I radio galaxies from a well-studied sample (see Section 2). Our primary focus is on continuum emission in the band covered by the Spitzer Space Telescope's Infrared Spectrograph. We analyze archival spectra using a pair of specialized fitting codes based on Markov Chain Monte Carlo (MCMC) techniques. We seek to determine whether there is evidence for obscuration consistent with the clumpy torus model by Nenkova et al. (2002) in a sample of 10 nearby low-luminosity radio galaxies. We used MCMC fitting

Table 1
Basic Sample Information

UGC Number	NGC Number	Alternate Name	R.A. (J2000.0)	Decl. (J2000.0)	Redshift
597	315		$00^h\ 57^m\ 48\overset{s}{.}9$	$+30^d\ 21^m\ 09^s$	0.016485
689	383	3C 31	$01^h\ 07^m\ 24\overset{s}{.}9$	$+32^d\ 24^m\ 45^s$	0.017005
1004	541		$01^h\ 25^m\ 44\overset{s}{.}3$	$-01^d\ 22^m\ 46^s$	0.018086
1841		3C 66B	$02^h\ 23^m\ 11\overset{s}{.}4$	$+42^d\ 59^m\ 31^s$	0.021258
6635	3801		$11^h\ 40^m\ 16\overset{s}{.}9$	$+17^d\ 43^m\ 41^s$	0.011064
6723	3862	3C 264	$11^h\ 45^m\ 05\overset{s}{.}0$	$+19^d\ 36^m\ 23^s$	0.021718
7360	4261	3C 270	$12^h\ 19^m\ 23\overset{s}{.}2$	$+05^d\ 49^m\ 31^s$	0.007378
7494	4374	M84, 3C 272.1	$12^h\ 25^m\ 03\overset{s}{.}7$	$+12^d\ 53^m\ 13^s$	0.003392
7654	4486	M87, 3C 274	$12^h\ 30^m\ 49\overset{s}{.}4$	$+12^d\ 23^m\ 28^s$	0.004283
11718	7052		$21^h\ 18^m\ 33\overset{s}{.}0$	$+26^d\ 26^m\ 49^s$	0.015584

Note. Redshifts, R.A., and decl. by Anderson & Ulvestad (2005) and accessed from the NASA/IPAC Extragalactic Database.

algorithms to fit spectral lines and decompose the underlying spectra to IR observations.

We provide an overview of the concepts involved and previous evidence surrounding the possibility of nucleus obscuration in this section. We then describe our sample of FR I radio galaxies in Section 2, followed by an overview of the archival data used in this research in Section 3, along with the processing of our broadband ancillary data. In Section 4 we provide our analysis of the narrow spectral features in the Spitzer/IRS spectra for each source, with particular focus on AGNs and star formation tracers and the 10 and 18 μm silicate features. In Section 5 we show the results of fitting various spectral energy distribution models to our entire broadband data set for each source and provide upper limits on any possible torus component (or equivalent MIR thermal component) in those sources that do not require one. In Section 6 we discuss the implications of the models that best agree with the observations and compare our results to those of previous authors.

2. Sample

Our sample is the subset from a list compiled by Verdoes Kleijn et al. (1999) for which there exist low-resolution CASSIS spectra (Lebouteiller et al. 2011, see Section 3). We list basic information about the sample galaxies in Table 1. The Verdoes Kleijn et al. (1999) sample consists of all nearby ($v_r < 7000\,\mathrm{km\,s^{-1}}$) radio galaxies in the Nilson (1973) Uppsala General Catalogue (UGC) with decl. $-5° < \delta < 82°$ that are $\geqslant 10''$ at 3σ in VLA A Array maps (to exclude compact sources) and brighter than 150 mJy at 1400 MHz. This sample was extracted from a catalog of 176 radio galaxies (Condon & Broderick 1988) constructed through position coincidence between their Green Bank 1400 MHz sky maps (Condon & Broderick 1985, 1986, 1988) and the UGC. Condon & Broderick (1988) distinguished between starburst sources and AGN-powered "monsters" based on radio morphology, infrared−radio parameter $\log(S_{60\mu m}/S_{1400\mathrm{MHz}})$, and infrared spectral index. Xu et al. (1999) provide a detailed description of this sample's radio properties. We summarize past measurements of the 1.4 GHz radio luminosity density, central black hole mass estimate, Eddington luminosity, and the logarithm of the core-extended brightness ratio (which is an indicator for AGN orientation in unified models) from the literature for our sample in Table 2. We additionally show the luminosity distance and scale inferred from the redshift, assuming each object's motion is dominated by the Hubble flow using a flat ΛCDM cosmology, in Table 3. We use these scales and angular extents of each radio source from the literature to estimate the physical extent of each radio source, which we show in Table 4.

Table 2
1.4 GHz Radio Luminosity Density, Black Hole Mass Estimate, Eddington Luminosity, and Logarithm of Core-extended Brightness Ratio (an Indicator for AGN Orientation in Unified Models) for FR I AGNs in Our Sample

Source	$L_{\nu,1.4\mathrm{GHz}}$ (10^{31} erg s^{-1} Hz^{-1})	M_{BH} ($10^8\,M_\odot$)	L_{Edd} (10^{47} erg s^{-1})	$\log_{10}R_c$
NGC 315	1.26	14.6	1.84	−0.39
3C 31	3.24	9.24	1.16	−1.34
NGC 541	0.871	2.03	0.226	⋯
3C 66B	8.71	18.6	2.34	−1.29
NGC 3801	0.309	1.53	0.193	⋯
NGC 3862	5.62	4.66	0.587	−1.00
3C 270	2.51	7.75	0.976	−1.44
M84	0.224	7.30	0.920	−1.18
M87	7.94	22.5	2.84	−1.24
NGC 7052	0.110	3.62	0.456	−0.22

Note. $L_{\nu,1.4\mathrm{GHz}}$ by Condon & Broderick (1988), M_{BH} by Noel-Storr et al. (2007) based on a relation by Merritt & Ferrarese (2001), and $\log_{10}R_c$ by Kharb & Shastri (2004).

Table 3
Distance and Scale Information for Sample

Source	Redshift	Luminosity Distance (Mpc)	Scale (kpc arcsec^{-1})
NGC 315	0.016485	71.50	0.3466
3C 31	0.017005	73.78	0.3577
NGC 541	0.018086	78.54	0.3808
3C 66B	0.021258	92.53	0.4486
NGC 3801	0.011064	47.79	0.2317
NGC 3862	0.021718	94.57	0.4585
3C 270	0.007378	31.78	0.1541
M84	0.003392	14.56	0.07059
M87	0.004283	18.40	0.08921
NGC 7052	0.015584	76.54	0.3711

Note. We calculated luminosity distances from redshifts using conversion software by the Astropy Collaboration et al. (2013) for a flat ΛCDM cosmology with Hubble constant $H_0 = 70\,\mathrm{km\,s^{-1}}$ and an energy density composition of 30% ordinary baryonic matter and dark matter ($\Omega_{\mathrm{M}} = 0.3$) and 70% dark energy ($\Omega_\Lambda = 0.7$).

Table 4
Largest Extent of Radio Source

Source	Angular Extent	Physical Extent (Mpc)	References
NGC 315	52′	1.1	Mack et al. (1997)
3C 31	45′	0.96	Laing et al. (2008)
NGC 541	3′	0.068	Bogdán et al. (2011)
3C 66B	11.′5	0.310	Hardcastle et al. (1996)
NGC 3801	40	0.0093	Heesen et al. (2014)
NGC 3862	8.′7	0.239	Bridle & Vallee (1981)
3C 270	7.′8	0.072	Kolokythas et al. (2015)
M84	3.′142	0.01331	Laing & Bridle (1987)
M87	13.′9	0.0744	Owen et al. (2000)
NGC 7052	2′	0.044	Morganti et al. (1987)

The original paper on this sample by Verdoes Kleijn et al. (1999) investigated broad- and narrowband images of 19 of the 21 radio galaxies in its sample from the Wide-Field Planetary Camera 2 aboard HST. Kleijn et al. (2002) searched the same sample for relations between radio and optical continua and optical Hα + [N II] emission. Noel-Storr et al. (2003) analyzed midresolution spectra of emission-line-emitting gas in FR I nuclei from the Space Telescope Imaging Spectrograph aboard HST. Noel-Storr et al. (2007) followed up on this with further analysis of the gas kinematics in the same spectra in order to assess the viability of using gas disk kinematics to estimate central black hole masses. Verdoes Kleijn & de Zeeuw (2005) compared dust distributions and their relation to radio jet orientation in the cores of the UGC FR I sample to two comparison samples. Capetti et al. (2005) looked at HST optical narrowband images of emission-line regions in a sample of 47 galaxies, which includes the FR I UGC sample. The most recent study on the UGC FR I sample was by Kharb et al. (2012). They examined 1.6 and 5 GHz images of 19 out of the 21 radio galaxies from the Very Large Baseline Array, as well as archival Chandra X-ray images of 14 sources and new Chandra X-ray images of UGC 408.

3. Archival Data

All data for this analysis are archival observations. The central data set is a set of 10 low-resolution Spitzer/IRS spectra that cover the wave band where a clumpy torus is expected to be the brightest. Since the nucleus is not resolved by Spitzer/IRS, we also need to constrain the contribution from the host galaxy. The stellar population models are constrained by photometry from the Two Micron All Sky Survey (2MASS) and Spitzer/IRAC, which extend the band from the IRS short-wave limit of ∼5 μm out to ∼1 μm, where stellar emission is more prominent. To constrain emission from the interstellar medium (ISM), we use photometry from Spitzer/MIPS and Herschel/SPIRE (where available) to extend our coverage from the IRS long-wave limit of ∼35 μm out to ∼500 μm. In this section we describe the processing of each of these data sets in order of increasing wavelength.

2MASS, as described by Skrutskie et al. (2006), was a *J*-, *H*-, and *K*-band survey covering 99.998% of the sky performed between 1997 June and 2001 February. Observations were performed by two 1.3 m telescopes in Mount Hopkins, Arizona, USA, and in Cerro Tololo, Chile. The point-source extractions used an instantaneous point-spread function width of 4″ with sky background subtraction in an annulus with an inner radius of 14″ and an outer radius of 20″. Extended source extractions used a fiducial ellipse determined by the 20 mag arcsec^{-2} isophote for each source. We list the semimajor axes for these ellipses in Table 5. Both sets of extractions are described in detail by Cutri et al. (2003).

For 2MASS data we use point-source extractions of our target AGN as a lower bound to the estimated flux that would pass through an aperture the size of the Spitzer/IRS SL module's aperture and extended source extractions as an upper bound. This is because the nucleus itself should be an unresolved point source, whereas emission from the host galaxy will dominate on larger scales. 3C 66B is not in the 2MASS Extended Source Catalog, so we replaced it with extended source photometry by Lilly et al. (1985).

Our Spitzer/IRAC data are archival images from the Spitzer Heritage Archive. For reference we show the instrument specifications for Spitzer/IRAC from Werner et al. (2004) and Fazio et al. (2004) in Table 6. We list the astronomical observation request key (AORKEY) for each source in Table 7, with the exception of M87, for which we show the ancillary photometry in Table 8. For each source we performed a point-spread function fit to provide a lower bound to the flux and an aperture extraction with the same 4″ aperture as 2MASS as an upper bound. Both extractions were centered on the CASSIS source centroid. For this purpose we used the Overlap, Mosaicking, and Multiframe aperture extraction of the Mosaicking and Point Source Extraction (MOPEX) software by Makovoz & Marleau (2005) to combine the IRAC frames (and later MIPS frames) into one mosaic and perform aperture photometry on the result. All 10 sources had usable images for channel 2 (effective wavelength $\lambda_{\rm eff} = 4.493$ μm), and all but M84 had usable images for channel 1 ($\lambda_{\rm eff} = 3.550$ μm). We list the IRAC photometry in Tables 9 and 10.

All of our IRS spectra, which cover a total wavelength coverage from 5.3 to 38 μm, are tapered column extractions from the low-resolution catalog of the Combined Atlas of Sources with Spitzer/IRS Spectra (CASSIS, formerly the Cornell Atlas of Spitzer/IRS Sources) by Lebouteiller et al. (2011).

Similar to our Spitzer/IRAC data, our Spitzer/MIPS data are archival images from the Spitzer Heritage Archive for which we list the AORKEY in Table 7. The photometry extraction pipeline for MIPS in MOPEX is also similar to that for IRAC. However, the aperture extraction module in MOPEX failed, so we used the point-source flux only. The point-spread function for the 70 and 160 μm bands is wider than for IRS, so the point-source flux provided an upper bound on the far-infrared flux of our fits. Only M84 had no usable MIPS photometry and NGC 3801 had no usable 70 μm data. Unfortunately, although MIPS had spectroscopic capabilities, there were no MIPS spectra for the galaxies in our sample.

The Spectral and Photometric Imaging Receiver (SPIRE) aboard Herschel has imaging bands at wavelengths of 250, 350, and 500 μm with FWHM beam widths of 18″, 25″, and 36″ respectively. SPIRE also has an imaging Fourier transform spectrometer, but, as with Spitzer/MIPS, only photometry observations are available of any of our sample galaxies.

We used archival Herschel/SPIRE point-source extractions from the SPIRE Point Source Catalog by Marton et al. (2016). We list the observation identification number (obsid) for the two sources in Table 7. The SPIRE Point Source Catalog

Table 5
2MASS Extended Source Extraction Information

Source	Semimajor Axis (arcsec)	J, 1.235 μm (ap. mag)	H, 1.662 μm (ap. mag)	K_s, 2.159 μm (ap. mag)
NGC 315	65.6	9.044 ± 0.012	8.301 ± 0.016	8.050 ± 0.017
3C 31	49.9	9.619 ± 0.014	8.894 ± 0.018	8.599 ± 0.023
NGC 541	37.8	10.462 ± 0.017	9.772 ± 0.026	9.484 ± 0.034
3C 66B[a]	…	…	…	…
NGC 3801	49.9	9.999 ± 0.013	9.264 ± 0.020	9.004 ± 0.020
NGC 3862	30.7	10.707 ± 0.021	9.976 ± 0.025	9.720 ± 0.034
3C 270	79.9	8.355 ± 0.016	7.652 ± 0.016	7.407 ± 0.017
M84	115.0	7.260 ± 0.015	6.587 ± 0.016	6.222 ± 0.023
NGC 7052	61.9	9.628 ± 0.012	8.934 ± 0.015	8.653 ± 0.020

Notes. Semimajor axes refer to the K_s-band 20 mag arcsec^{-2} isophotal fiducial ellipse used in the extraction.
[a] Not in extended source catalog.

Table 6
IRAC Instrument Specifications

Channel	Isophotal Wavelength[a] (μm)	Bandpass (μm)	Mean FWHM (arcsec)
1	3.550	3.19–3.94	1.66
2	4.493	4.00–5.02	1.72
3	5.731	4.98–6.41	1.88
4	7.872	6.45–9.34	1.98

Notes. Based on the work of Werner et al. (2004) and Fazio et al. (2004).
[a] See definition by Fazio et al. (2004)—in short, the isophotal wavelength is the wavelength assigned to the flux density of the broadband measurement.

Table 7
Spitzer AORKEYs for Ancillary Data Used in Our Analysis

Source	IRAC AOR	MIPS AOR
NGC 315	19169024	4427776
3C 31	14805760	21681920/4691968[a]
NGC 541	19170048	4345088
3C 66B	14806016	10927360
NGC 3801	19170304	19168512
NGC 3862	14807552	4692480
3C 270	14807808	4692736
M84	4671744	4692992
NGC 7052	18257664	19168768

Notes. M87 photometry came from a different data set (see Table 8), and so that object is excluded from this table.
[a] Due to an issue with channel 1 in 4691968, we use the channel 1 data from 21681920 for our analysis of 3C 31.

Table 8
Ancillary Photometry Data for M87

Wavelength (μm)	Flux (mJy)	Aperture (arcsec)	Limit	Reference
1.25	227. ± 3.	14	Upper	Skrutskie et al. (2006)
1.25	78. ± 2.	7.5	Lower	Frogel et al. (1978)
1.64	284. ± 4.	14	Upper	Skrutskie et al. (2006)
1.65	98. ± 3.	7.5	Lower	Frogel et al. (1978)
2.17	237. ± 3.	14	Upper	Skrutskie et al. (2006)
2.20	77. ± 2.	7.5	Lower	Frogel et al. (1978)
4.49	24.2	5.8	Lower	Teplitz et al. (2012)
71.3	480 ± 40	18	Upper	Temi et al. (2009)
156	580 ± 10	40	Upper	Shi et al. (2007)
250	900 ± 200	18	Upper	Baes et al. (2010)
350	1000 ± 300	25	Upper	Baes et al. (2010)
500	1400 ± 400	36	Upper	Baes et al. (2010)

reports fluxes and not magnitudes, so no further processing is necessary. We summarize all our ancillary data in Tables 9 and 10 with the previously mentioned exception of M 87 which is shown in Table 8.

4. Spectral Feature Fitting

We have developed a modified version of PAHFIT (Smith et al. 2007), pahfitMCMC, to measure narrow spectral features and subtract them from Spitzer/IRS spectra. These narrow-line features include mainly fine-structure lines and rovibrational transitions of H_2. The challenge is that narrow lines are undersampled in low-resolution IRS spectra and may sit atop broad spectral features such as PAH emission or silicate (10 and 18 μm) absorption or emission, which makes continuum subtraction difficult. PAHFIT uses well-established models for PAH and silicate features, in addition to models for starlight and thermal dust continuum, to provide an estimate of the spectral baseline for narrow-line features.

In pahfitMCMC, there are two primary modifications over the original PAHFIT. First, we include additional spectral features that may contribute to the infrared spectra of AGNs, namely, high-ionization fine-structure lines and a simple model for optically thin, warm silicate emission (Gallimore et al. 2010). Second, we adopted an MCMC approach to parameter estimation. Fitting a Spitzer/IRS spectrum in this way involves allowing the code to take random steps through parameter space; for this purpose, we used the DREAM(Z) algorithm of ter Braak & Vrugt (2008), which efficiently samples high-dimensional parameter spaces. Solutions were accepted or rejected using the Metropolis algorithm (Metropolis et al. 1953). Initial, out-of-equilibrium solutions were identified by inspection of posterior log-likelihood chains and discarded. The best-fit solutions for parameters such as line strength and equivalent width are determined by averages and standard deviations of the posterior chains.

In summary, pahfitMCMC reports fitted line strengths and equivalent widths for narrow emission lines, fitted line strengths and equivalent widths for PAH and silicate features, a line-subtracted spectrum for each source (to which we fit

Table 9
Ancillary Photometry for First Five Sources Sorted by R.A.

Source	Channel	Limit	IRAC Flux (mJy)	MIPS Flux (mJy)	SPIRE Flux (mJy)
NGC 315	1	Upper	23.20 ± 0.01	⋯	⋯
		Lower	10.02 ± 0.02	⋯	⋯
	2	Upper	14.93 ± 0.01	342. ± 6.	⋯
		Lower	7.65 ± 0.02	⋯	⋯
	3	Upper	⋯	471. ± 3.	⋯
3C 31	1	Upper	21.99	⋯	954. ± 5.
		Lower	8.69 ± 0.01	⋯	⋯
	2	Upper	13.45	439. ± 2.	423. ± 5.
		Lower	5.046	⋯	⋯
	3	Upper	⋯	931. ± 5.	170. ± 6.
NGC 541	1	Upper	12.26 ± 0.01	⋯	80 ± 10
		Lower	5.87 ± 0.01	⋯	⋯
	2	Upper	7.437 ± 0.006	125. ± 3.	40 ± 10
		Lower	3.56 ± 0.01	⋯	⋯
	3	Upper	⋯	82. ± 3.	60 ± 60
3C 66B	1	Upper	10.72	⋯	⋯
		Lower	4.70 ± 0.05	⋯	⋯
	2	Upper	6.545 ± 0.003	⋯	⋯
		Lower	2.21 ± 0.004	⋯	⋯
NGC 3801	1	Upper	15.79	⋯	⋯
		Lower	8.40 ± 0.01	⋯	⋯
	2	Upper	9.417 ± 0.005	⋯	⋯
		Lower	4.787 ± 0.008	⋯	⋯
	3	Upper	⋯	1154. ± 3.	⋯

Note. Continued for four out of five remaining sources in Table 9.

Table 10
Ancillary Photometry for All Remaining Sources Not Included in Table 9 except for M87

Source	Channel	Limit	IRAC (mJy)	MIPS (mJy)	SPIRE (mJy)
NGC 3862	1	Upper	14.09	⋯	⋯
		Lower	7.838 ± 0.006	⋯	⋯
	2	Upper	9.265 ± 0.003	192. ± 3.	⋯
		Lower	5.878 ± 0.006	⋯	⋯
	3	Upper	⋯	233. ± 2.	⋯
3C 270	1	Upper	43.32 ± 0.02	⋯	200 ± 10
		Lower	17.57 ± 0.02	⋯	⋯
	2	Upper	25.45 ± 0.01	144.4 ± 0.7	200 ± 20.
		Lower	10.50 ± 0.01	⋯	⋯
	3	Upper	⋯	155. ± 2.	200 ± 20
M84	1	Upper	⋯	⋯	250 ± 20
	2	Upper	41.53 ± 0.02	⋯	150 ± 20
		Lower	21.49 ± 0.02	⋯	⋯
	3	Upper	⋯	⋯	140 ± 20
NGC 7052	1	Upper	20.12 ± 0.01	⋯	⋯
		Lower	8.38 ± 0.01	⋯	⋯
	2	Upper	12.07	400. ± 7.	⋯
		Lower	5.23 ± 0.01	⋯	⋯
	3	Upper	⋯	812. ± 5.	⋯

Note. We show the ancillary photometry for M87 in Table 8.

continuum models in Section 5; the simple continuum models at this step are not diagnostic), and Bayesian marginalized error estimates for all fits. We show pahfitMCMC fits for our sample in Figure 1, show a labeled example of the spectral fits from Figure 1 in Figure 2 for clarity, and then discuss important diagnostics.

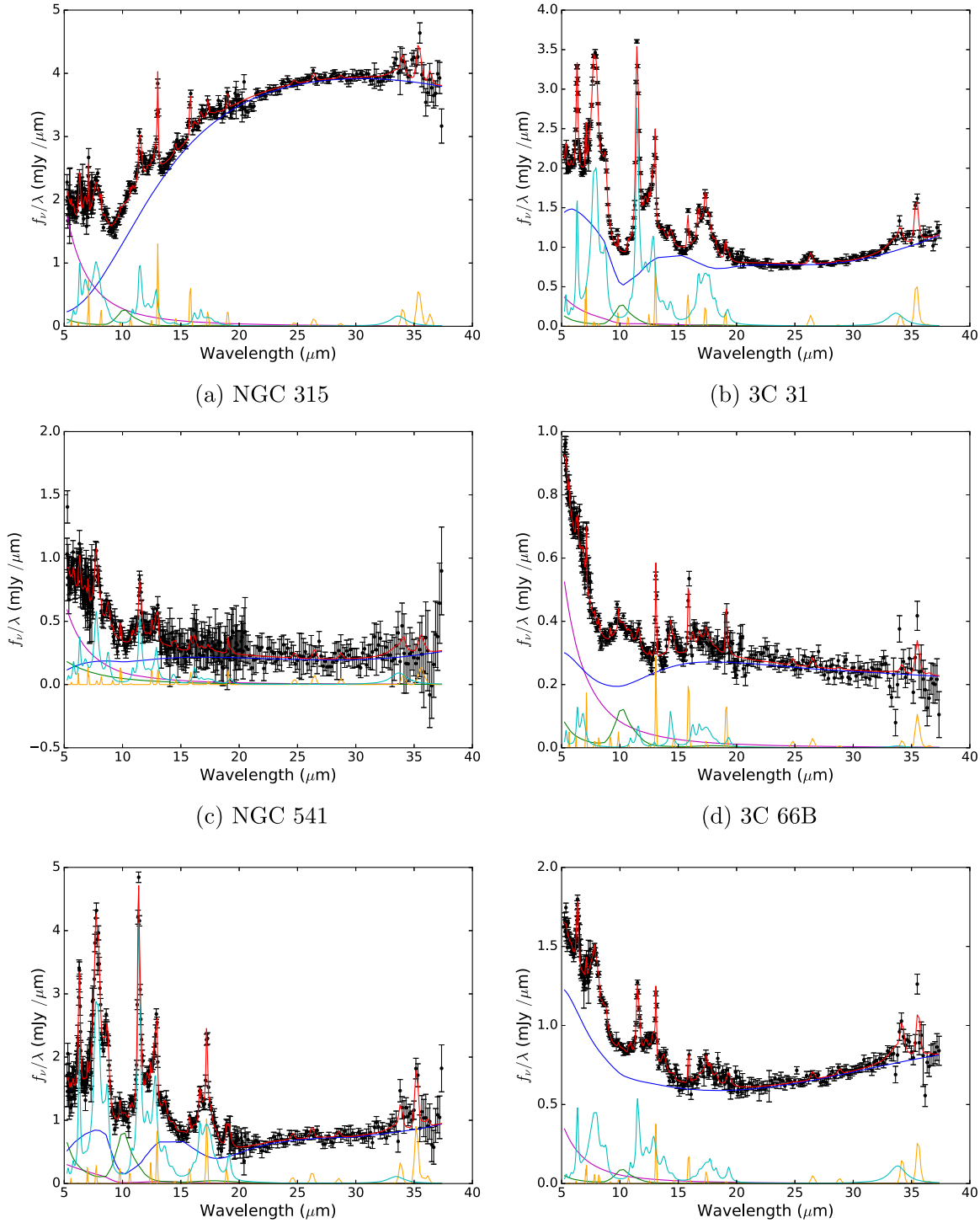

(a) NGC 315 (b) 3C 31

(c) NGC 541 (d) 3C 66B

(e) NGC 3801 (f) NGC 3862

Figure 1. Spectral line fits for six of the sample galaxies. In each fit the red line is the total fit, the dark-blue line is the line-subtracted spectral energy distribution minus any power-law component, the purple line is a power-law component (likely associated with the Rayleigh–Jeans tail of starlight), the green line represents the silicate features, light blue represents PAH lines, and yellow represents the narrow ionization lines. Shown here in radiant flux per unit frequency f_ν per unit wavelength λ because photon energy is linear with frequency and infrared spectroscopy is done in wavelength space. To convert to the more standard νf_ν form in W m^{-2}, multiply by 10^{-26} c $= 2.998 \times 10^{-12}$ μm s^{-1}.

4.1. Star Formation Rate Estimates

We use $L_{[\mathrm{Ne\ II}]}$ and $L_{[\mathrm{Ne\ III}]}$, the luminosities of [Ne II] and [Ne III] lines, respectively, to estimate the SFR in each sample galaxy, which we show in Table 11. This estimate by Ho & Keto (2007), $\mathrm{SFR_{Ne}}$, is given as

$$\mathrm{SFR_{Ne}} = 4.73 \times 10^{-41}\, M_\odot\ \mathrm{yr^{-1}\ s\ erg^{-1}} \times [L_{[\mathrm{Ne\ II}]} + L_{[\mathrm{Ne\ III}]}]. \quad (1)$$

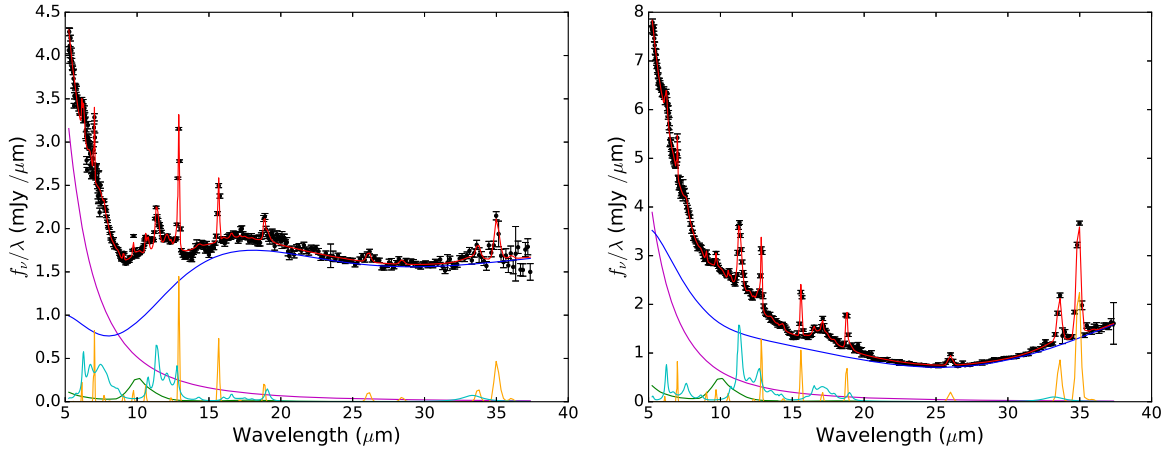

(g) 3C 270 (h) M 84

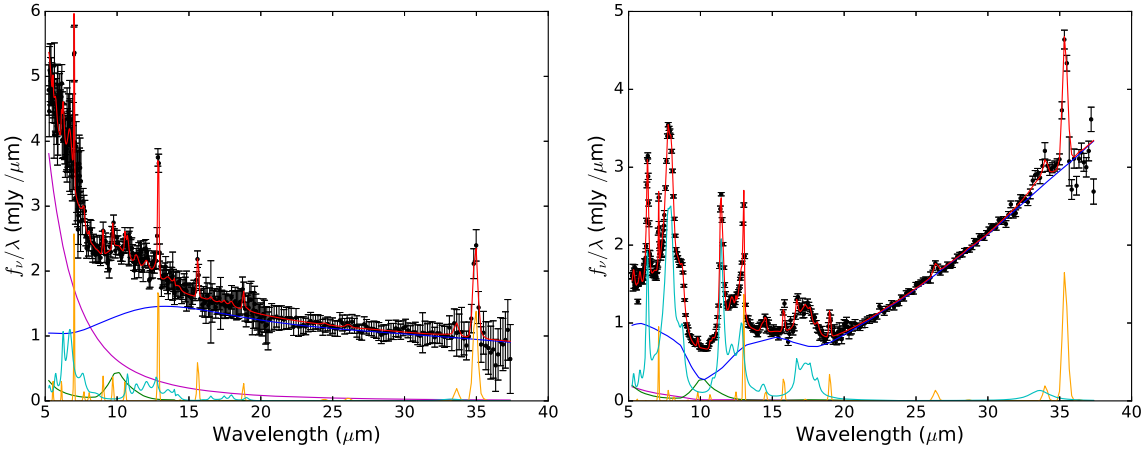

(i) M 87 (j) NGC 7052

Figure 1. (Continued.)

Similarly, we use the combined luminosity of the 6.2 and 11.3 μm PAH lines, $L_{\rm PAH}$, to get a second independent estimate of the SFR in each source. This estimate by Farrah et al. (2007), $\rm SFR_{PAH}$, is given by

$$\rm SFR_{PAH} = 1.18 \times 10^{-41}\, M_\odot\ yr^{-1}\, s\ erg^{-1}\, [L_{PAH}]. \quad (2)$$

Finally, we also show SFR estimates in Table 11 using scalings by Roussel et al. (2001) using 7 μm ($L_{7\mu\rm m}$) and 15 μm ($L_{15\mu\rm m}$) "photometry" measurements created by integrating the Spitzer/IRS spectra over 16.18 and 6.75 THz bandpasses, respectively, to approximate the bandpasses of the relevant Infrared Space Observatory filters. These scalings are given by

$$\rm SFR_{7\mu m} = 6.3 \times 10^{-43}\, M_\odot\ yr^{-1}\, s\ erg^{-1}\, [L_{7\mu m}] \quad (3)$$

and

$$\rm SFR_{15\mu m} = 1.7 \times 10^{-42}\, M_\odot\ yr^{-1}\, s\ erg^{-1}\, [L_{15\mu m}], \quad (4)$$

with ∼50% calibration uncertainties. Farrah et al. (2007) showed that Equations (1) and (2) give equivalent results in their Figure 15; this is also supported by Willett et al. (2010). However, Jensen et al. (2017) found that AGN activity can dominate PAH emission in Seyfert galaxies, and it is currently unknown whether this finding will generalize to include low-luminosity radio galaxies. Despite the different estimates, they are consistently below a few solar masses per year, so we do not expect star formation to contribute a large thermal component in the MIR, which could be mistaken for warm nuclear obscuring material.

The high $\rm SFR_{PAH}$ estimates in 3C 31 and NGC 3862 are consistent with the high PAH emission Leipski et al. (2009) found in these objects. Our relatively low $\rm SFR_{PAH}$ estimates in 3C 66B and 3C 270 are also consistent with their findings of no PAH features in 3C 66B and weak PAH features in 3C 270. However, Leipski et al. (2009) found significant 11.3 μm PAH emission in M84, which is inconsistent with our results.

4.2. High-ionization Lines

Significant emission lines from ionization states with a high ionization potential require a large source of high-energy photons. These photons can come from massive stars, but the central engine itself is the obvious photon source candidate. Indeed, Spinoglio & Malkan (1992) showed that you can distinguish star formation from accretion based on which lines are excited; AGNs produce photons that can ionize atoms with a higher ionization potential. We list the luminosities of four

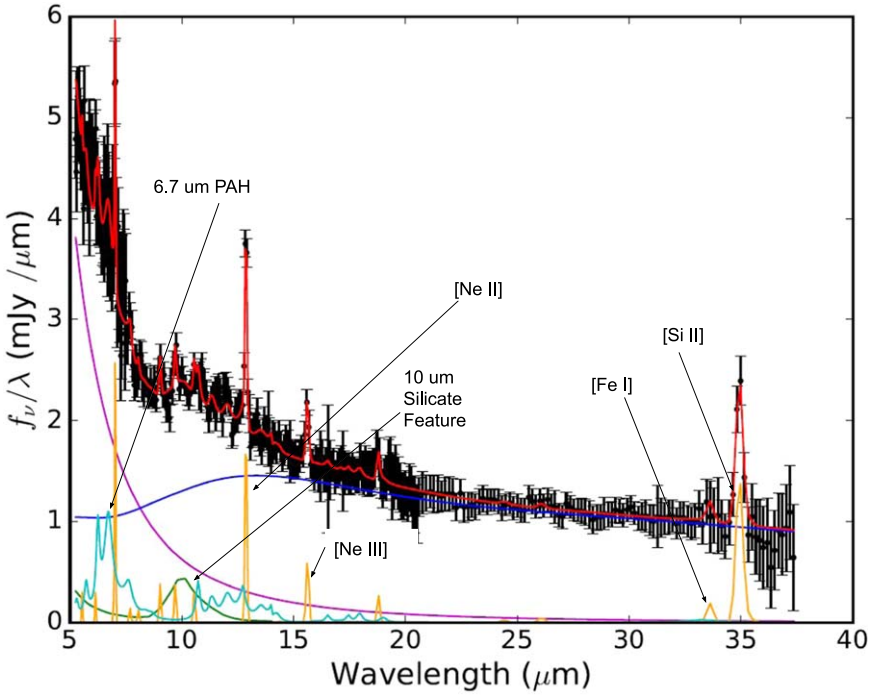

Figure 2. Spectral line fit for M87 from Figure 1, with some large or important spectral features labeled. As before, the red line is the total fit, the dark-blue line is the line-subtracted spectral energy distribution minus any power-law component, the purple line is a power-law component, the green line represents the silicate features, light blue represents PAH lines, and yellow represents the narrow ionization lines.

Table 11
SFR Estimates for Each Source Based on Narrow Emission Features

Source	SFR_{PAH} ($M_\odot$ yr^{-1})	SFR_{Ne} ($M_\odot$ yr^{-1})	$SFR_{7\mu m}$ ($M_\odot$ yr^{-1})	$SFR_{15\mu m}$ ($M_\odot$ yr^{-1})
NGC 315	1.6 ± 0.9	1.6 ± 0.9	0.2 ± 0.1	0.4 ± 0.2
3C 31	4. ± 2.	1.0 ± 0.5	0.9 ± 0.4	1.1 ± 0.5
NGC 541	0.9 ± 0.5	0.2 ± 0.1	1.2 ± 0.6	1.4 ± 0.7
3C 66B	0.3 ± 0.2	0.7 ± 0.4	0.9 ± 0.5	3. ± 2.
NGC 3801	2. ± 1.	0.4 ± 0.2	0.4 ± 0.2	0.5 ± 0.2
NGC 3862	1.5 ± 0.8	0.8 ± 0.4	0.4 ± 0.2	0.6 ± 0.
3C 270	0.2 ± 0.1	0.3 ± 0.2	3. ± 1.	8. ± 4.
M84	0.09 ± 0.05	0.10 ± 0.05	0.5 ± 0.2	0.5 ± 0.3
M87[a]	1. ± 1.	6. ± 3.	1.1 ± 0.5	1.3 ± 0.7
NGC 7052	3. ± 2.	1.2 ± 0.6	0.09 ± 0.04	0.09 ± 0.05

Notes. Estimated uncertainties on Roussel et al. (2001) 7 and 15 μm estimates are dominated by calibration uncertainties inferred from the Roussel et al. (2001) 7 and 15 μm–Hα relation and Kennicutt (1998) Hα–SFR relation for a total uncertainty of ∼50%. Note how even the highest of these estimates is on the order of a few solar masses per year, which suggests that star formation is not likely to be a significant contributor to the overall spectral energy distribution of any galaxy in our sample.
[a] Donahue et al. (2011) found that some brightest cluster galaxies show elevated [Ne II] owing to contributions from a cooling intracluster medium. This may explain the discrepant estimates of SFR in M87.

high-ionization lines that are accretion tracers in Table 12: [Ne VI] 8 μm, [Ne V] 14 μm, [Ne V] 24 μm, and [O IV] 26 μm. High-energy ionizing photons from an accretion disk should be unable to penetrate a dusty obscuring torus, so the detection of infrared spectral lines from highly ionized species suggests that we are seeing unobscured or minimally obscured (in infrared) emission from clouds near the central engine. Note that the presence of these lines does not completely prohibit an obscuring torus, since these lines are infrared radiation that can pass through dust clouds better than UV or optical photons from the central engine. Still, they suggest that some other explanation may be preferable.

4.3. Silicate Constraints on Torus Models

We compare our 10 and 18 μm silicate feature observations to model sets by Sirocky et al. (2008) to test whether our results are consistent with clumpy torus models, as this is an important diagnostic of the clumpiness of an obscuring torus. We show this comparison in Figure 3, where we compare our best-fit silicate line strengths S_{sil}, defined as

$$S_{sil} = \log\left(\frac{f_{obs}}{f_{cont}}\right), \quad (5)$$

in terms of the observed flux of the feature f_{obs} and the interpolated continuum flux f_{cont} at the peak wavelength, that we found in our line fits to the various Sirocky et al. (2008) clumpy torus and smooth shell models.

Nenkova et al. (2008b) model the radial distribution of the clumpy torus N_r as the power-law distribution

$$N_r \propto r^{-q}. \quad (6)$$

Figures 3(a)–(c) show the comparison to model sets, each with various numbers N of clouds along the line of sight, by Sirocky et al. (2008) with power-law index q of 0–2, respectively.

Similarly, the mass distribution of the single continuous cloud in the smooth shell model also follows a power law,

$$\rho_r \propto r^{-q}, \quad (7)$$

still described by the power-law index, q, and dependent on the radial extent of the cloud, Y (given in units of the dust sublimation radius).

Table 12
High-ionization Line Luminosities

Source	$L_{[\mathrm{Ne\ VI}]}$ 8 μm (10^{39} erg s^{-1})	$L_{[\mathrm{Ne\ V}]}$ 14 μm (10^{39} erg s^{-1})	$L_{[\mathrm{Ne\ V}]}$ 24 μm (10^{39} erg s^{-1})	$L_{[\mathrm{O\ IV}]}$ 26 μm (10^{39} erg s^{-1})
NGC 315	<5.9	<4.8	<3.0	<5.0
3C 31	<5.2	<3.3	<0.82	3.5 ± 0.7
NGC 541	<5.8	<7.9	<4.7	<6.3
3C 66B	<2.3	<3.6	<2.0	<3.1
NGC 3801	<11.	<2.	<3.8	<3.2
NGC 3862	<5.4	<2.2	<2.9	<4.1
3C 270	0.35 ± 0.08	<0.49	<0.27	<0.92
M84	<0.13	<0.21	<0.033	$0.32^{+0.04}_{-0.06}$
M87	<1.4	<0.70	<0.54	<0.75
NGC 7052	$4. \pm 1.$	<12.	<2.0	<7.6

Note. The majority of entries are upper limits on nondetections. Note that the higher upper limits here are not restrictive; they would miss emission at the same luminosity as detected lines in other sources.

We find that the silicate line strengths are inconsistent with smooth shell models of AGN obscuration and with clumpy models with power-law indices $q > 1$ and are consistent with clumpy models with $q \leqslant 1$ and $N \leqslant 5$, although a few are also consistent with the complete absence of any 18 μm silicate feature. Note that in Section 5 we find that only 4 of our 10 sources show a significant thermal component in their continua, which we denote with blue and yellow markers in Figures 3(a)–(c).

5. Continuum Fitting

The infrared spectra, including low-resolution, narrow-line-subtracted IRS spectra, were decomposed using clumpyDREAM (Sales et al. 2015). This software assumes that the infrared spectra of active galaxies include contributions from starlight, dusty star-forming regions, obscuring molecular clouds near the AGN, etc. (see, e.g., Genzel & Cesarsky 2000). To decompose the observed infrared spectrum, clumpyDREAM simultaneously fits models for these different infrared sources. During the fit, gridded model parameters are allowed to vary smoothly over the range allowed by the model grid, and a model spectrum is extracted from the model grid by n_p-dimensional spline interpolation, where n_p is the number of parameters defining the model grid.

clumpyDREAM uses a custom implementation of the DREAM(ZS) MCMC stepper algorithm (ter Braak & Vrugt 2008) to fit models to the observed spectra. The DREAM(ZS) stepper uses differential evolution, as described by Storn & Price (1997), to determine most of its steps in parameter space, but it uses the snooker updater described by ter Braak & Vrugt (2008) for every 10th iteration. It uses ∼100 walkers randomly initialized with uniform priors (Sales et al. 2015). For further details on clumpyDREAM and further overview of DREAM(ZS), see the appendix of Sales et al. (2015).

Fitting a spectrum was performed in two stages. First, we used a modified version of clumpyDREAM, clumpyDREAM-BIC, to determine which model components are likely needed to best fit the observed spectrum. To this end, clumpyDREAMBIC searches for best-fit model combinations with different model components (e.g., starlight, star-forming regions, etc.) toggled off or on. A given model combination is evaluated for goodness of fit using the Bayesian information criterion (BIC; Schwarz 1978),

$$\mathrm{BIC} = -2 \ln \mathcal{L} + k \ln n, \tag{8}$$

where $\mathcal{L}$ is the likelihood function, k is the number of parameters in the trial set of model components, and n is the number of data points in the observed spectrum. By searching for model combinations that minimize the BIC, the result is a model that maximizes the likelihood function while penalizing model combinations that overfit the observed spectrum (i.e., too large k). After clumpyDREAMBIC estimates the BIC for different combinations of model components, the fit is repeated with for fixed sets of model components in clumpyDREAM. A typical run for a single spectrum involves first running clumpyDREAMBIC with three parallel chains for 10^6 iterations with chains thinned by a factor of 10 (i.e., parameter values are stored to the Markov chains every 10 iterations). Then, based on the output of clumpyDREAMBIC, clumpyDREAM is run on fixed model combinations, again with three parallel chains, 10^6 iterations, and factor of 10 thinning.

In this section we describe each of the model components we try to fit with clumpyDREAM except for the clumpy torus model itself, which we describe in Section 1.1. For quick reference we list all of these and their source papers in Table 13.

These targets are galaxies, so we force the model to include a simple stellar population for every source, as well as a diffuse ISM. We use the GRASIL stellar population model for elliptical galaxies developed by Silva et al. (1998) and the diffuse ISM model described by Draine & Li (2007). The GRASIL models simulate a 1 Gyr burst of star formation followed by passive evolution and so are described solely by the age and scaling of the stellar population. The stellar population models are not expected to contribute significantly in the IRS band, but they should dominate the near-IR (NIR) and so should be well constrained by our 2MASS and IRAC photometry. Our results in some cases favor models in which stars contribute significantly to the IRS band, particularly at the short-wavelength end, but this is not surprising owing to the dim nucleus. In this section, however, there is significant contribution from the stellar population model through the short-wave end of the IRS band in several of our sources, which is likely due to the low overall IRS band luminosity of those sources.

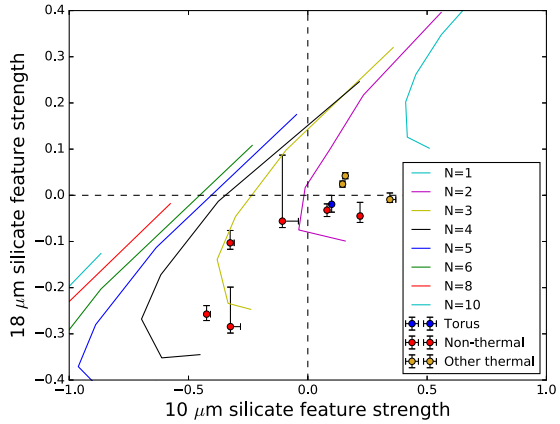

(a) Clumpy torus model, $q = 0$

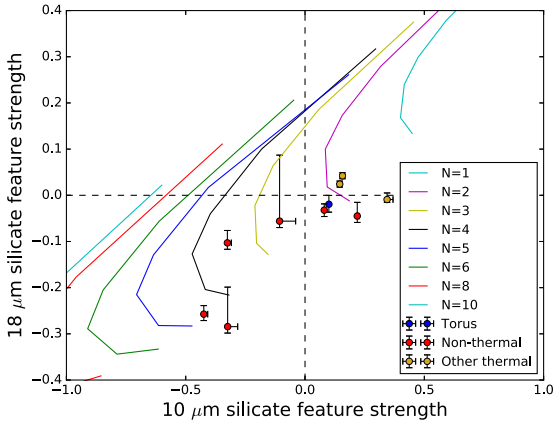

(b) Clumpy torus model, $q = 1$

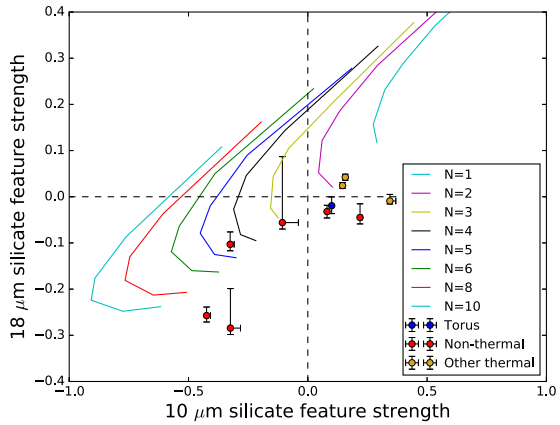

(c) Clumpy torus model, $q = 2$

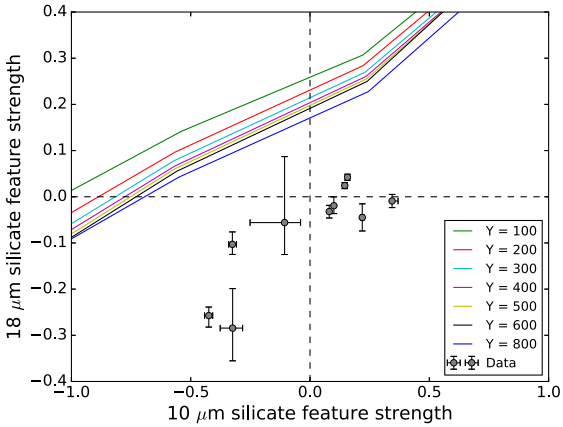

(d) Smooth shell model, $q = 0$

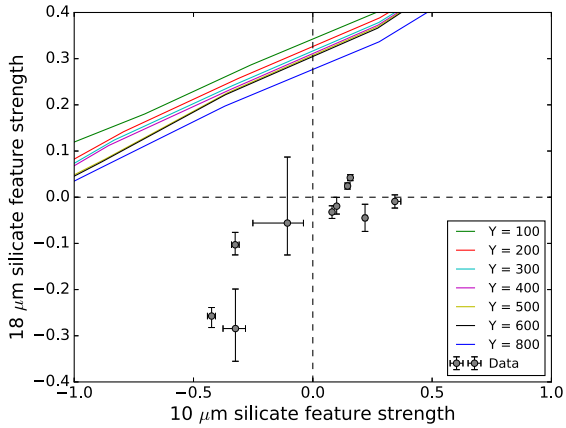

(e) Smooth shell model, $q = 1$

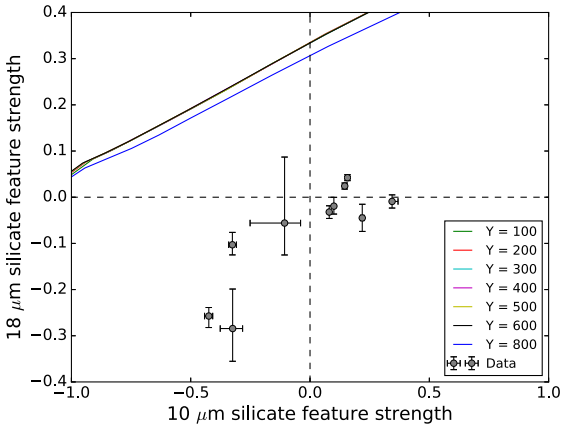

(f) Smooth shell model, $q = 2$

Figure 3. Comparison of silicate absorption/emission strengths to predictions of various smooth and clumpy torus models. Y is given in units of the dust sublimation radius. Note that there is significant overlap between the region occupied by the clumpy torus models with $q = 0$ and the region occupied by the data. There is less overlap between the data and the $q = 1$ clumpy torus models and no significant overlap with any other model sets. Galaxies with thermal components (torus, NLR, and/or hot dust) in our continuum fits (see Section 5) are flagged with different colors in the clumpy torus model plots.

The diffuse ISM model by Draine & Li (2007) has three main parameters: the mass fraction of polycyclic aromatic hydrocarbons (PAHs) $q_{\rm PAH}$ relative to the total dust mass, the lower limit of the interstellar radiation field as a scaling of that in the solar neighborhood $U_{\rm min}$, and photodissociation regions exposed to $U_{\rm max} = 10^6 U_{\rm min}$ that are characterized by their relative contribution γ to the spectrum.

We use a narrow-line region (NLR) model, based on the DUSTY continuum radiative transfer code by Nenkova et al. (1999), together with an $800\,{\rm K} \leqslant T \leqslant 1600\,{\rm K}$ blackbody hot dust model. This approach is similar to the one taken by Mor et al. (2009) in order to fit IRS spectra of quasi-stellar objects. Mor et al. (2009) also attempted torus models and models with both a torus and an NLR and found that neither were adequate.

Table 13
All Spectrum Model Components We Considered

Component	Plotting Color	Reference
Clumpy torus	Green	Nenkova et al. (2008b)
Hot dust	Pink	⋯
Cold dust	⋯	⋯
Diffuse ISM	Blue	Draine & Li (2007)
Simple stellar population	Yellow	Silva et al. (1998)
Foreground extinction on torus	⋯	Fischera et al. (2003)
Power law	Purple	⋯
Narrow-line region	Cyan	Nenkova et al. (1999)
Aperture correction	⋯	⋯

Note. Extinction and aperture correction are not plotted as model components; they alter other model components. No sources require a cold dust component; however, our far-infrared data are only upper limits. The "hot dust" and "cold dust" components are blackbodies.

Since we are extending our data set beyond the IRS band into the far-infrared/submillimeter, we consider a cold dust component as well. All three components are described in our models by two parameters each—their temperature and their luminosity. Note that the NLR clouds and hot dust are optically thin.

We also try a foreground extinction component, as described by Fischera et al. (2003), on the torus in 3C 31, NGC 3801, and M84. These sources appear to have regions with decreased brightness compared to adjacent regions at the same radius that could be foreground dust in Sloan Digital Sky Survey (SDSS) images by Blanton et al. (2017), although it is only obvious in NGC 3801. On a similar note, we only tested power-law synchrotron spectra in sources with known optical/IR jets. These are 3C 31 (Lanz et al. 2011), 3C 66B (Tansley et al. 2000), NGC 3862 (Crane et al. 1993), and M87 (Perlman et al. 2001). We constrain the power-law indices to the widest ranges given in the cited papers. We list these model components in Table 13 for reference.

In this section we present the best-fit models for the continuum emission from each of our sample galaxies. Additionally, we present the results of forcing a torus component and suppressing all other IR-peaked thermal components (i.e., requiring that the software include a clumpy torus component and not include any other thermal components that peak in IR) in order to establish a firm upper limit on the contribution to the total flux from a possible torus component. Low contributions from a compact clumpy torus may otherwise be hidden by fitting degeneracies between thermal model components; removing the possibility of such fitting degeneracies allows us to determine the highest contribution from a torus component to the overall spectrum that would still be consistent with observations. Finally, we present an overview of the results for the entire sample at the end of this section.

5.1. NGC 315

This source favors a torus component, and that torus component is a significant part of the best fit, contributing ∼70% of the flux at 15 and 30 μm and ∼50% at 60 μm. There is possible degeneracy between the torus component and NLR component, but we doubt that this is a significant concern in this case owing to the fact that the BIC will penalize the torus model more harshly as a result of its higher number of parameters. We therefore see no particular reason to doubt the presence of an obscuring warm torus-like structure in this AGN. We summarize the best-fit parameters for this source in Table 14 and show the best-fit spectral decomposition in Figure 4.

Table 14
Fractional Contributions of the Various Model Components to the Overall Continuum in NGC 315

Component	Wavelength (μm)	Best Fit (%)	Minimum (%)	Maximum (%)
Torus	5.0	1.4	0.8	33.5
	15.0	69.0	59.4	97.8
	30.0	69.9	40.8	100
	60.0	47.8	13.5	91.9
Diffuse ISM	5.0	1.8	0.2	2.9
	15.0	10.4	1.7	20.1
	30.0	24.7	1.7	64.9
	60.0	50.1	4.2	100
Stars	5.0	96.8	58.8	100
	15.0	20.6	2.1	22.8
	30.0	5.4	0.2	6.0
	60.0	2.0	0.0	2.2

Table 15
Fractional Contributions of the Various Best-fit Model Components to the Overall Continuum in 3C 31

Component	Wavelength (μm)	Best Fit (%)	Minimum (%)	Maximum (%)
Diffuse ISM	5.0	4.2	3.0	5.0
	15.0	57.0	43.2	64.4
	30.0	83.6	65.7	100
	60.0	99.1	18.7	100
Stars	5.0	95.8	83.0	100
	15.0	43.0	27.2	64.6
	30.0	16.4	5.6	25.0
	60.0	0.9	0.2	1.2

The presence of a torus component in the spectral energy distribution of NGC 315 is consistent with the discovery of broad polarized Hα emission in this source by Barth et al. (1999), which may indicate the presence of a Thomson-scattered hidden broad-line region.

Similarly, Gu et al. (2007) detected a low-luminosity compact AGN in IRAC and MIPS images of NGC 315 after removal of stellar IR emission and accounting for emission from a central dusty disk. They make no claims about the nature of this AGN; however, its presence is consistent with our result that the IR spectrum of NGC 315 is not entirely dominated by emission from the host galaxy.

5.2. 3C 31

This source appears to be dominated by emission from the host galaxy in the IRS band. This source contains an optical jet, first noticed by Butcher et al. (1980), and a radio jet that Croston et al. (2003) identifies as the same structure as in the optical. The optical jet does not contribute substantially to the IR core flux. It is worth noting, however, that Lanz et al. (2011) detect extended NIR emission from the jet at kiloparsec scales in Spitzer/IRAC images. We summarize the best-fit parameters for this source in Table 15 and show the best-fit spectral decomposition in Figure 5. As shown in Figure 6 and in Table 16, when a torus

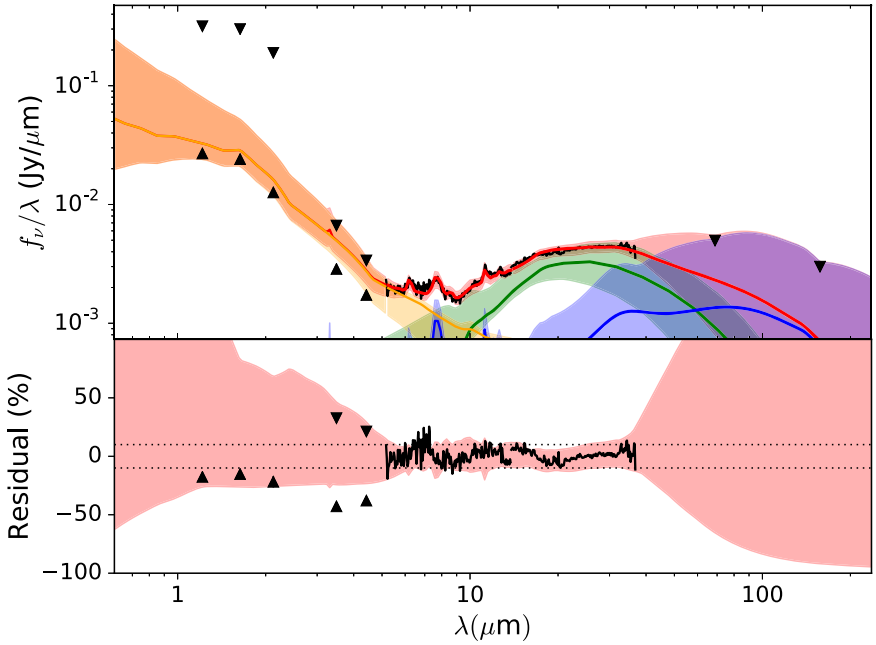

Figure 4. Best continuum fit for NGC 315. The model consists of a simple stellar population (yellow), diffuse ISM (blue), and clumpy torus (green). The total fit is shown in red, although in the NIR it appears as orange owing to overlap with the stellar population.

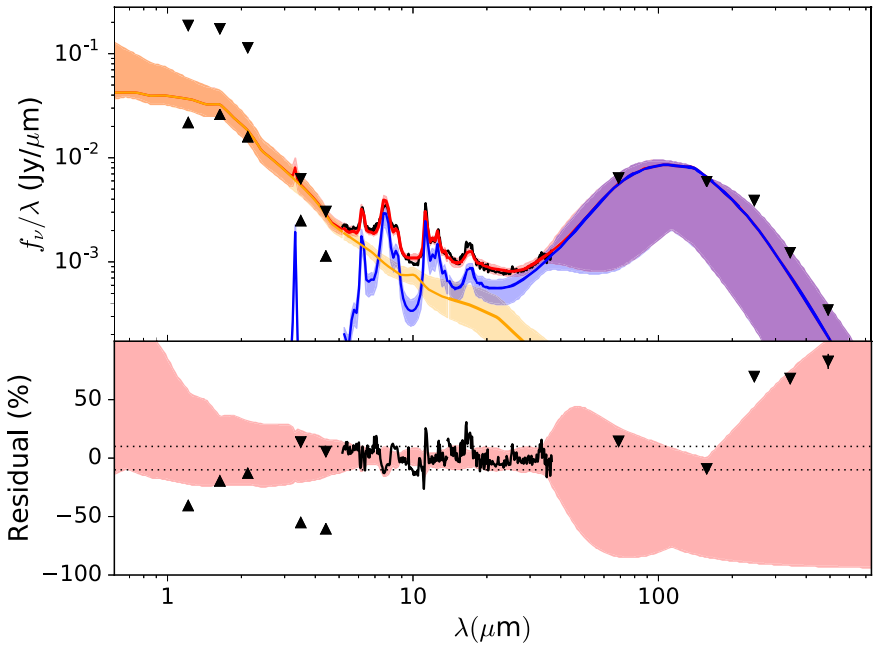

Figure 5. Best continuum fit for 3C 31. The model consists of a simple stellar population (yellow) and diffuse ISM (blue). The total fit is shown in red, although in the NIR it appears as orange owing to overlap with the stellar population. This is the only source with a complete data set.

component is forced it contributes a significant amount of flux at 15 and 30 μm, with best-fit fractional contributions of 34.2% and 18.7%, respectively. However, the BIC difference between galaxy models with a forced torus (425.7) and galaxy-only models (403.5) is nonnegligible (the BIC of the forced-torus model is 22.2, or ∼6%, higher), and we notice no obviously unphysical best-fit model parameters; therefore, we conclude that we do not find evidence for a warm obscuring torus in the infrared spectra of 3C 31. We note, however, that Constantin et al. (2015) detected broad Hα emission with an FWHM of 2710 km s^{-1}, contributing 86% of the combined narrow+broad Hα flux. This broad Hα is consistent with the presence of a broad-line region and therefore possibly an accretion disk.

5.3. NGC 541

Not only does the best fit (as shown in Figure 7 and Table 17) to the continuum emission in this source not require a torus component, but the best-fit contribution from a forced-torus component is also not significant, contributing only ∼20% at its brightest, as shown in Table 18 and Figure 8. The largest difference between the best-fit model and the data is the

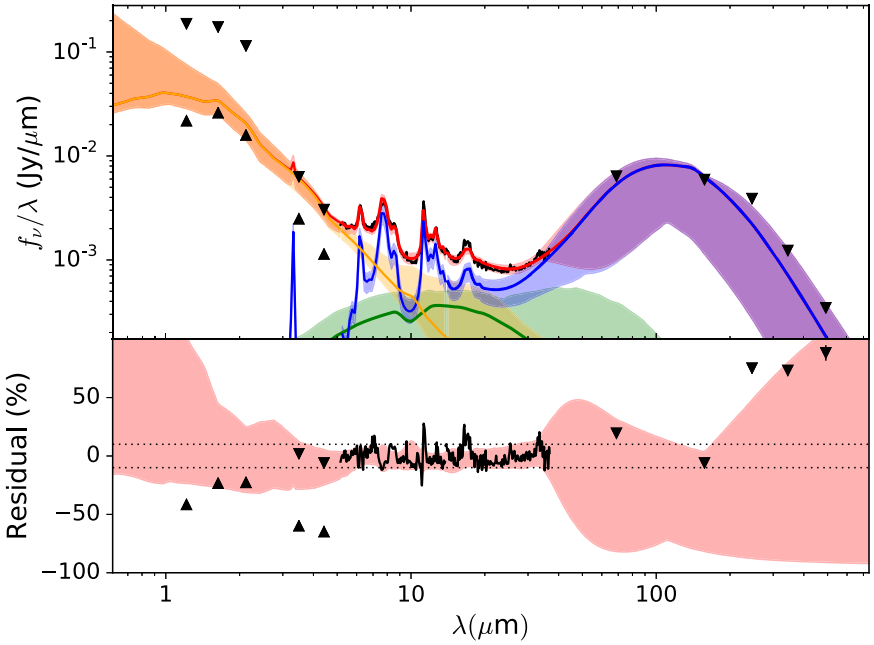

Figure 6. Continuum fit for 3C 31 forcing a torus component (green). The model is otherwise the same as in Figure 5.

Table 16
Fractional Contributions of the Various Model Components to the Overall Continuum in 3C 31 with a Forced-torus Component

Component	Wavelength (μm)	Best Fit (%)	Minimum (%)	Maximum (%)
Torus	5.0	8.0	0.0	13.6
	15.0	34.2	0.0	48.7
	30.0	18.7	0.0	54.2
	60.0	0.4	0.0	11.2
Diffuse ISM	5.0	3.6	2.8	4.4
	15.0	51.1	39.6	59.3
	30.0	77.9	45.2	98.4
	60.0	99.4	19.9	100
Stars	5.0	88.4	73.5	98.9
	15.0	14.8	8.0	59.3
	30.0	3.4	1.2	24.7
	60.0	0.2	0.0	1.3

70 μm, but that point is an upper limit and the best-fit model is within the uncertainty of the data point. We therefore conclude that we can explain all the emission with only contributions from the host galaxy and none from the nucleus and so rule out any significant MIR-bright obscuration.

5.4. 3C 66B

The best fit for this source, as shown in Figure 9 and Table 19, requires a prominent hot dust component and a significant NLR model component. The best fit to the diffuse ISM component is unusually dim, but the uncertainties are wide.

The upper limit provided by the fit with a forced-torus component is a significant fraction of the total flux (see Table 20), but the forced torus is unusually cold and suppresses the diffuse ISM component (see Figure 10), and those two fits have a large BIC difference (best: 472.3; forced torus: 506.8) of 34.5. We note that the BIC difference may be primarily due to the removal of the hot dust component since we expect the most degeneracy between the NLR and torus components, as they are both MIR thermal components. Overall, we cannot rule out the possibility of a torus, especially given the presence of another MIR thermal component, but we also do not favor the presence of a torus, so we consider our results inconclusive with regard to the presence of a clumpy torus, but our results quite strongly indicate the presence of some MIR thermal component.

Table 17
Fractional Contributions of the Various Model Components to the Overall Continuum in the Best-fit Model of NGC 541

Component	Wavelength (μm)	Best Fit (%)	Minimum (%)	Maximum (%)
Diffuse ISM	5.0	2.0	0.9	2.5
	15.0	43.8	21.1	52.1
	30.0	82.1	36.3	100
	60.0	94.7	79.0	100
Stars	5.0	98.0	80.3	100
	15.0	56.2	33.0	100
	30.0	17.9	6.2	35.4
	60.0	5.3	1.3	10.1

5.5. NGC 3801

The best fit for NGC 3801, as shown in Figure 11 and Table 21, requires an NLR component; however, it is very dim, so we suspect that it is likely either a fitting artifact or possibly associated with a large-scale structure in the host galaxy. A likely candidate for this component from the host is the large dust lane visible near the AGN in HST images by Verdoes Kleijn et al. (1999). The forced-torus fit, shown in Table 22 and Figure 12, is significantly worse, with a BIC of 453.7 compared to the best-fit BIC of 423.5. We also show an extincted galaxy-only fit with a BIC of 437.3 in Figure 13 as a comparison since

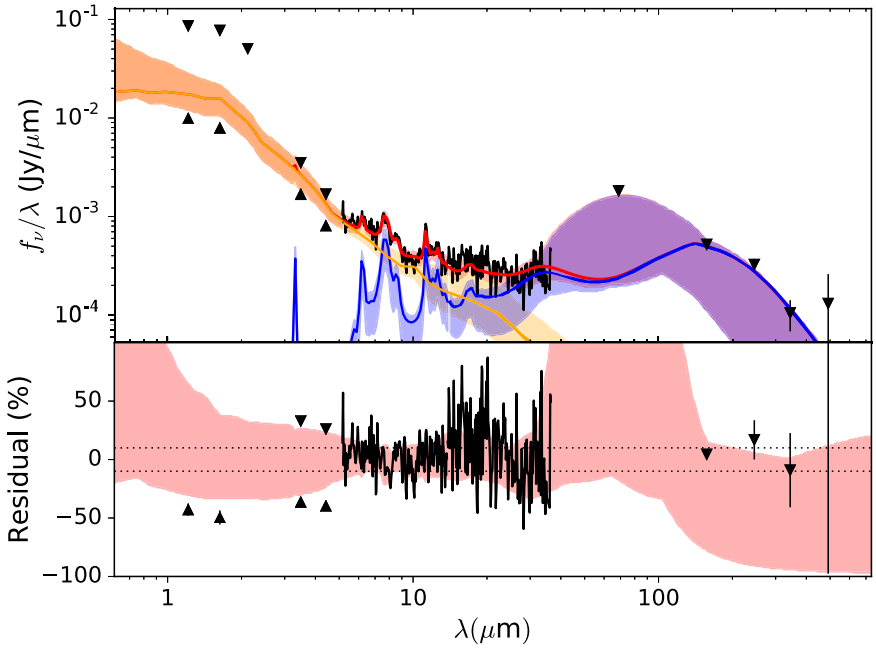

Figure 7. Best continuum fit for NGC 541. The model consists of a simple stellar population (yellow) and diffuse ISM (blue). The total fit is shown in red, although in the NIR it appears as orange owing to overlap with the stellar population. Upright triangles represent lower limits from photometry, and inverted triangles represent upper limits.

Table 18
Fractional Contributions of the Various Model Components to the Overall Continuum in NGC 541 with a Forced-torus Component

Component	Wavelength (μm)	Best Fit (%)	Minimum (%)	Maximum (%)
Torus	5.0	0.0	0.0	13.9
	15.0	4.3	0.0	78.8
	30.0	20.7	0.0	81.4
	60.0	15.7	0.0	100
Diffuse ISM	5.0	1.8	0.8	2.4
	15.0	36.8	20.2	51.4
	30.0	57.4	23.3	100
	60.0	78.6	39.9	100
Stars	5.0	98.1	74.6	100
	15.0	58.9	11.9	99.6
	30.0	21.9	1.7	40.1
	60.0	5.7	0.2	10.1

Table 19
Fractional Contributions of the Various Model Components to the Overall Continuum in the Best-fit Model for 3C 66B

Component	Wavelength (μm)	Best Fit (%)	Minimum (%)	Maximum (%)
Diffuse ISM	5.0	0.1	0.0	0.5
	15.0	5.9	0.1	11.8
	30.0	35.1	0.5	58.9
	60.0	66.7	1.1	100
Stars	5.0	64.0	31.4	83.2
	15.0	59.5	13.2	80.3
	30.0	28.7	3.1	38.6
	60.0	19.6	1.6	26.1
NLR	5.0	0.0	0.0	0.1
	15.0	26.1	11.6	49.2
	30.0	34.6	13.0	70.6
	60.0	12.9	4.4	48.2
Hot dust	5.0	35.9	8.8	84.5
	15.0	8.5	2.3	24.1
	30.0	1.7	0.4	5.1
	60.0	0.7	0.2	2.2

the dust lane that is a candidate thermal source would also provide foreground extinction on the core. Overall, we do not find evidence for nuclear obscuration in the form of a clumpy torus, and our results are ambiguous for any other warm thermal component in the nucleus itself owing to likely emission from the host galaxy.

Das et al. (2005) detected a flat-spectrum nonthermal core in NGC 3801 in 3 mm images from the Berkeley–Illinois–Maryland Association millimeter-wave array. This does not appear to contribute significantly to the IRS band, and we have too little far-infrared photometry to properly compare. They also detected carbon monoxide CO (1–0) emission from the dust disk seen in HST images (Verdoes Kleijn et al. 1999) with a velocity gradient indicating a ∼2 kpc rotating disk of molecular gas and dust with an inferred $3 \times 10^8 M_\odot$ of molecular hydrogen. They also detected a $\sim 10^8 M_\odot$ infalling molecular gas clump, which they attribute to a recent merger.

Hota et al. (2012) found evidence in GALEX images of a kinematically decoupled core in NGC 3801 in which star formation has recently declined following a post-merger burst but the jet-driven shock has not yet triggered a burst of star formation in the outer regions to the galaxy. In comparison, our SFR estimates based on PAH fit results in Section 4 are higher than average for our sample, and our SFR estimates based on narrow neon lines are typical for the sample. Our continuum models have a bright diffuse ISM, which may be associated with the large-scale gas Hota et al. (2012) predict will begin to

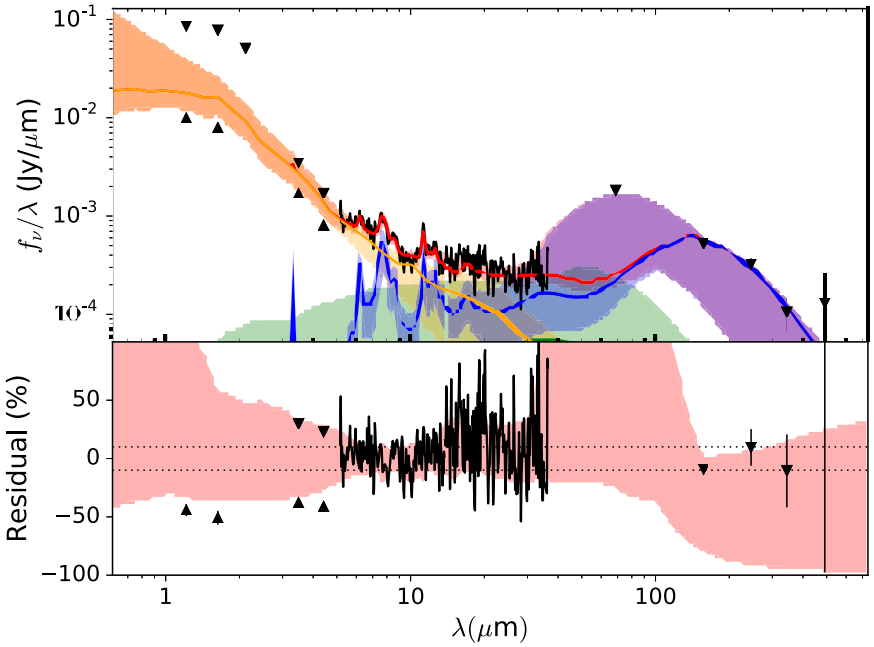

Figure 8. Continuum fit for NGC 541 forcing a torus component (green). The model is otherwise the same as in Figure 7.

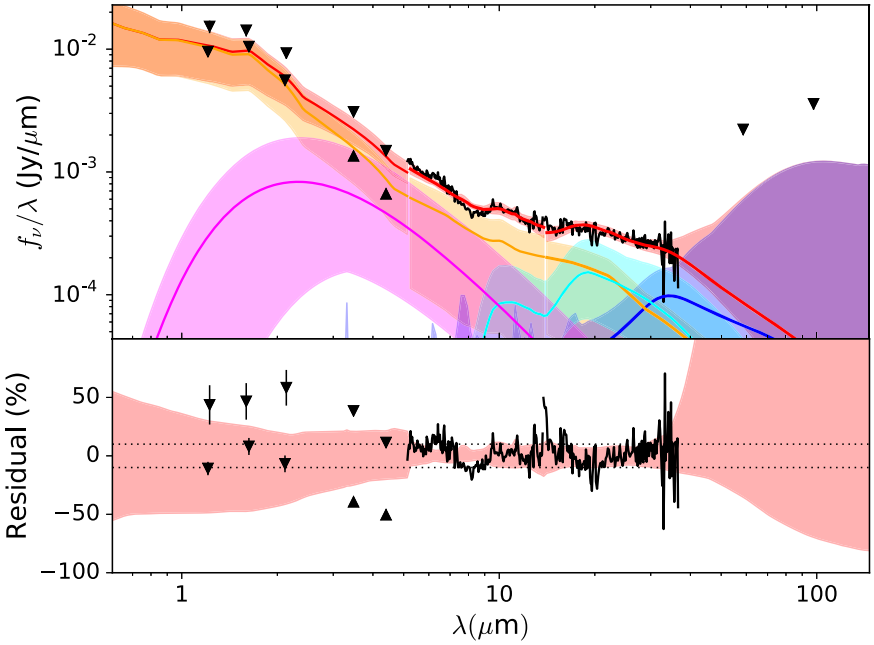

Figure 9. Best continuum fit for 3C 66B. The model consists of a simple stellar population (yellow), hot dust (pink), NLR (cyan), and diffuse ISM (blue). The total fit is shown in red, although in the NIR it appears as orange owing to overlap with the stellar population. We have applied aperture correction between the SL and LL regions. Upright triangles represent lower limits from photometry, and inverted triangles represent upper limits.

form stars within the next 10 Myr. Our stellar population models show a high stellar age of 9.4 Gyr, but as mentioned earlier, our model only accounts for one burst of star formation followed by passive evolution, so our results only suggest that the population of low-mass stars is still dominated by the older subpopulation.

5.6. NGC 3862

The best-fit model for this source, shown in Table 23 and Figure 14, requires only components from the host galaxy, suggesting that the AGN does not contribute significantly to the IR flux. The largest difference between the best-fit model and the data is the 70 μm, but that point is an upper limit and within the uncertainty on the best-fit model spectrum.

The forced-torus model in this source, shown in Figure 15 and Table 24, is quite reasonable albeit rather warm with a peak around 10 μm, providing a firm upper limit on any possible torus component of ∼17% of the flux at 5 μm, ∼50% of the flux at 15 μm, and ∼13% of the flux at 30 μm. However, it is also unnecessary to explain the infrared spectrum, as the best fit has a BIC of 391.9 and the forced-torus fit has a BIC of 420.3. Therefore, we see no evidence for a warm IR-bright obscuring structure in NGC 3862.

Table 20
Fractional Contributions of the Various Model Components to the Overall Continuum in 3C 66B with a Forced-torus Component

Component	Wavelength (μm)	Best Fit (%)	Minimum (%)	Maximum (%)
Torus	5.0	0.2	0.0	7.2
	15.0	26.7	11.4	50.0
	30.0	65.1	20.7	81.9
	60.0	78.7	17.2	100
Diffuse ISM	5.0	0.0	0.0	0.3
	15.0	0.0	0.0	7.7
	30.0	0.0	0.0	42.6
	60.0	0.1	0.0	100
Stars	5.0	99.8	90.9	100
	15.0	73.2	48.2	88.3
	30.0	34.9	22.5	41.8
	60.0	21.3	14.3	25.1

Table 21
Fractional Contributions of the Various Model Components to the Overall Continuum in the Best-fit Model for NGC 3801

Component	Wavelength (μm)	Best Fit (%)	Minimum (%)	Maximum (%)
Diffuse ISM	5.0	7.0	5.7	8.0
	15.0	79.6	64.2	88.2
	30.0	96.4	74.9	100
	60.0	99.9	19.7	100
Stars	5.0	85.9	69.5	99.6
	15.0	16.1	6.7	44.6
	30.0	2.8	1.0	17.8
	60.0	0.1	0.0	0.7
NLR	5.0	7.1	0.0	14.3
	15.0	4.3	0.0	21.3
	30.0	0.8	0.0	14.8
	60.0	0.0	0.0	10.5

Table 22
Fractional Contributions of the Various Model Components to the Overall Continuum in NGC 3801 with a Forced-torus Component

Component	Wavelength (μm)	Best Fit (%)	Minimum (%)	Maximum (%)
Torus	5.0	23.0	0.0	30.0
	15.0	13.0	0.0	34.2
	30.0	3.8	0.0	34.3
	60.0	0.0	0.0	13.1
Diffuse ISM	5.0	6.6	5.5	8.1
	15.0	76.7	61.2	87.2
	30.0	93.7	61.5	100
	60.0	99.9	18.2	100
Stars	5.0	70.4	58.6	100
	15.0	10.3	5.3	45.3
	30.0	2.5	0.8	18.7
	60.0	0.1	0.0	0.9

5.7. 3C 270

We show our best fit for 3C 270 in Figure 16, the best fit with a forced-torus component in Figure 17, and the fractional contributions to the flux in each of the two models in Tables 25 and 26, respectively. We suspect that the preference for an NLR model in this source is due to a bias in our analysis since BIC favors models with fewer parameters and the NLR model has fewer parameters than a clumpy torus model. Therefore, we cannot rule out a torus in this source. The presence of a torus in 3C 270 would be consistent with results by R. Antonucci

Table 23
Fractional Contributions of the Various Model Components to the Overall Continuum in the Best-fit Model for NGC 3862

Component	Wavelength (μm)	Best Fit (%)	Minimum (%)	Maximum (%)
Diffuse ISM	5.0	1.5	0.8	2.0
	15.0	30.1	21.2	37.6
	30.0	77.4	63.5	95.7
	60.0	93.3	54.8	100
Stars	5.0	98.5	89.2	100
	15.0	69.9	54.9	81.6
	30.0	22.6	10.2	26.1
	60.0	6.7	2.5	7.6

Table 24
Fractional Contributions of the Various Model Components to the Overall Continuum in NGC 3862 with a Forced-torus Component

Component	Wavelength (μm)	Best Fit (%)	Minimum (%)	Maximum (%)
Torus	5.0	16.7	0.0	27.3
	15.0	49.7	0.0	69.6
	30.0	13.0	0.0	68.5
	60.0	1.9	0.0	100
Diffuse ISM	5.0	1.3	0.5	2.0
	15.0	27.1	13.4	36.1
	30.0	78.1	12.4	87.6
	60.0	92.6	37.9	100
Stars	5.0	82.0	63.6	100
	15.0	23.2	8.1	82.4
	30.0	9.0	0.9	25.1
	60.0	5.5	0.2	12.1

Table 25
Fractional Contributions of the Various Model Components to the Overall Continuum in the Best-fit Model for 3C 270

Component	Wavelength (μm)	Best Fit (%)	Minimum (%)	Maximum (%)
Diffuse ISM	5.0	0.2	0.1	0.9
	15.0	5.0	2.9	17.2
	30.0	23.5	5.7	80.4
	60.0	90.3	7.7	94.5
Stars	5.0	99.8	93.1	100
	15.0	72.4	46.7	90.2
	30.0	29.8	18.1	37.0
	60.0	4.5	2.5	5.6
NLR	5.0	0.0	0.0	0.1
	15.0	22.6	3.1	37.4
	30.0	46.7	1.8	78.0
	60.0	5.2	0.1	15.6

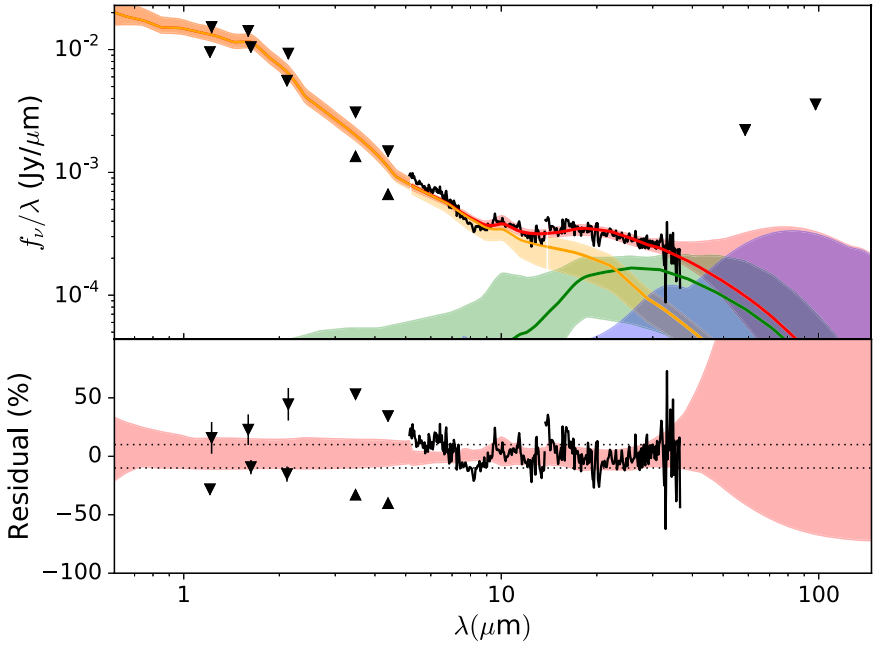

Figure 10. Continuum fit for 3C 66B forcing a torus component (green). To ensure maximal torus component, we excluded the NLR and hot dust components seen in Figure 9.

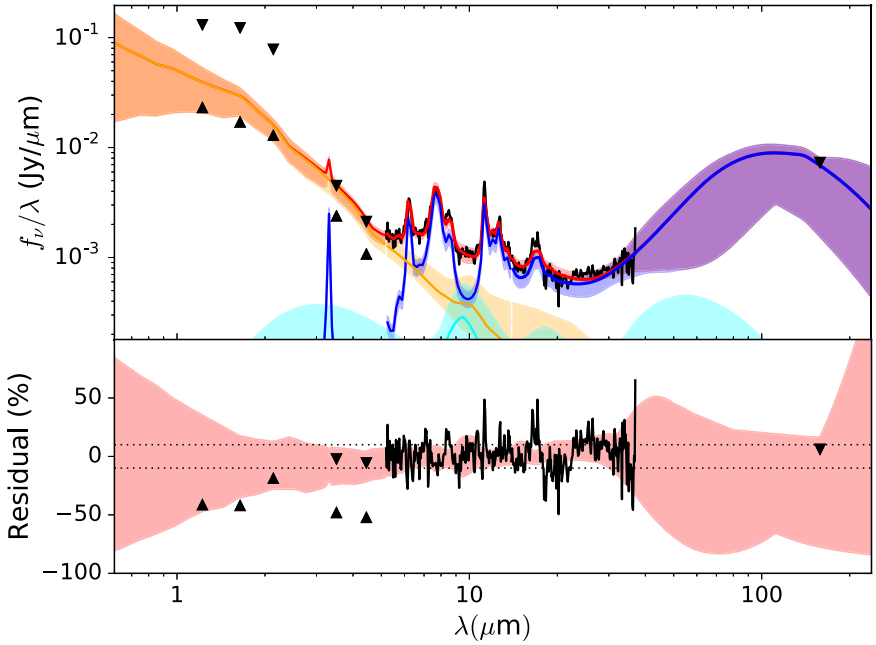

Figure 11. Best continuum fit for NGC 3801. The model consists of a simple stellar population (yellow), NLR (cyan), and diffuse ISM (blue). The total fit is shown in red, although in the NIR it appears as orange owing to overlap with the stellar population. Upright triangles represent lower limits from photometry, and inverted triangles represent upper limits.

(private communication), who detected broad polarized Hα emission. This is potentially indicative of a Thomson-scattered hidden broad-line region such as that expected in a high-excitation AGN; however, R. Antonucci (private communication) caution that it could instead be due to narrow lines in the complex. Additionally, although van der Wolk et al. (2010) ultimately do not conclude the existence of a warm MIR thermal component in any of the eight FR I radio galaxies in their sample, they list 3C 270 as a possible exception owing to a weak MIR consistent with 200 K dust. Jaffe et al. (1993) note a ∼60 pc disk of cold dust in HST images of 3C 270 surrounding its unresolved nucleus, the inner regions of which may be heated by the AGN (or star formation, but our SFR estimates are too low for that) to produce the MIR excess detected.

5.8. M84

We show the fractional contributions of each model component to the best-fit model in Table 27 and each component to the forced torus fits in Table 28. The best-fit model for this source, shown in Figure 18 with fractional contributions listed in Table 29, requires two AGN

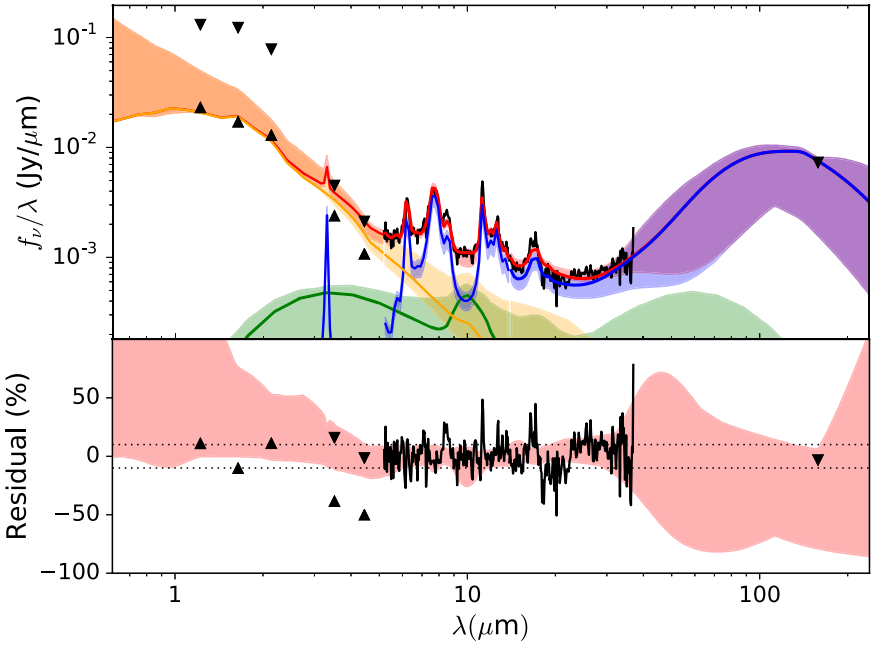

Figure 12. Continuum fit for NGC 3801 forcing a torus component (green). To ensure maximal torus component, we excluded an NLR component seen in Figure 11 from the fit.

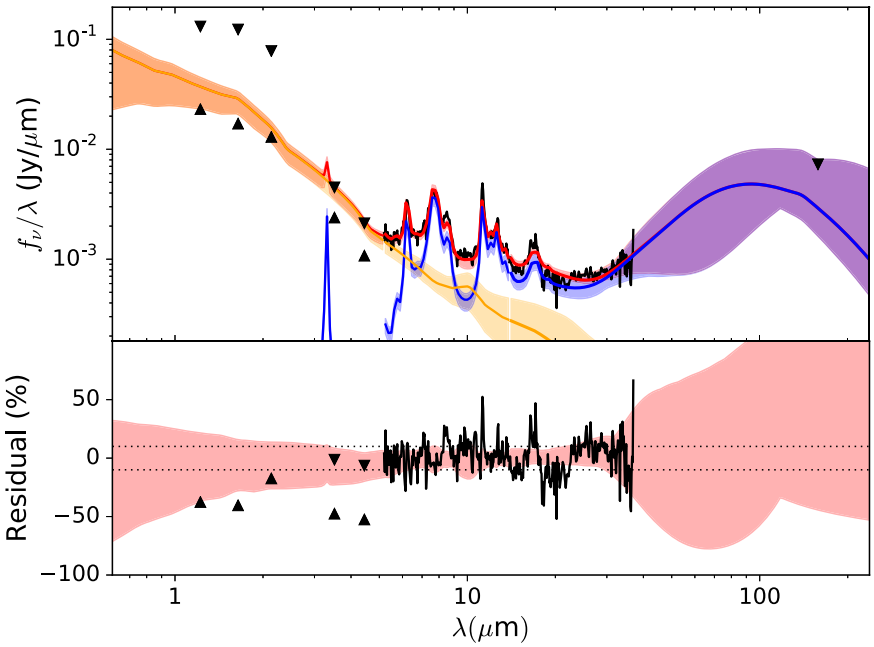

Figure 13. Galaxy-only continuum fit for NGC 3801. The model consists of a simple stellar population (yellow) and diffuse ISM (blue). The total fit is shown in red, although in the NIR it appears as orange owing to overlap with the stellar population. This is a somewhat poorer fit than that in Figure 11 and still better than the forced-torus fit in Figure 12. This model also requires a foreground extinction component. Upright triangles represent lower limits from photometry, and inverted triangles represent upper limits.

components: a hot dust component and an NLR. Unfortunately, we have no MIPS photometry and only one IRAC channel for M84.

The forced-torus component in the forced-torus fit to M84 (see Figure 19 and Table 30) is quite reasonable albeit unusually dim with a best-fit AGN luminosity of 1.2×10^{41} erg s^{-1} (see Table 38 and discussion in Section 6), and a peak best-fit fractional contribution to the spectrum of only 33.6% (see Table 28). However, it has the largest difference in goodness of fit out of any of our pairs of models, with the best fit having a BIC of 386.9 compared to 444.4 for the forced-torus fit. At least part of that is likely due to forced suppression of the hot dust component. Recall that the purpose of the forced-torus fits was to provide an upper limit on any potential torus contribution. Overall, we conclude that there is likely an optically thin thermal hot dust component and that the bumps in the spectrum toward the MIR are probably a thermal component, although likely not in the form of a Nenkova et al. (2002) clumpy torus.

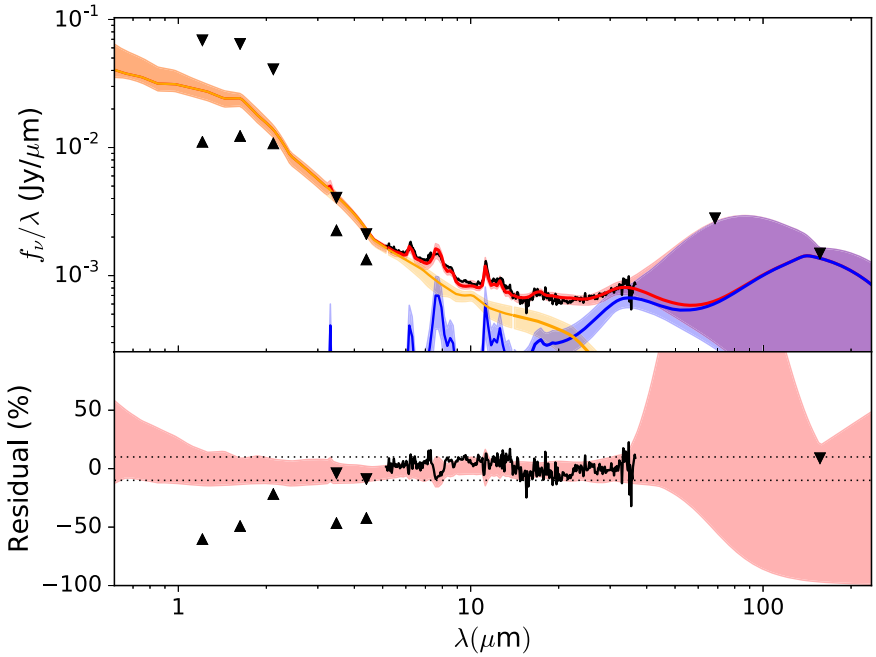

Figure 14. Best continuum fit for NGC 3862. The model consists of a simple stellar population (yellow) and diffuse ISM (blue). The total fit is shown in red, although in the NIR it appears as orange owing to overlap with the stellar population. Upright triangles represent lower limits from photometry, and inverted triangles represent upper limits.

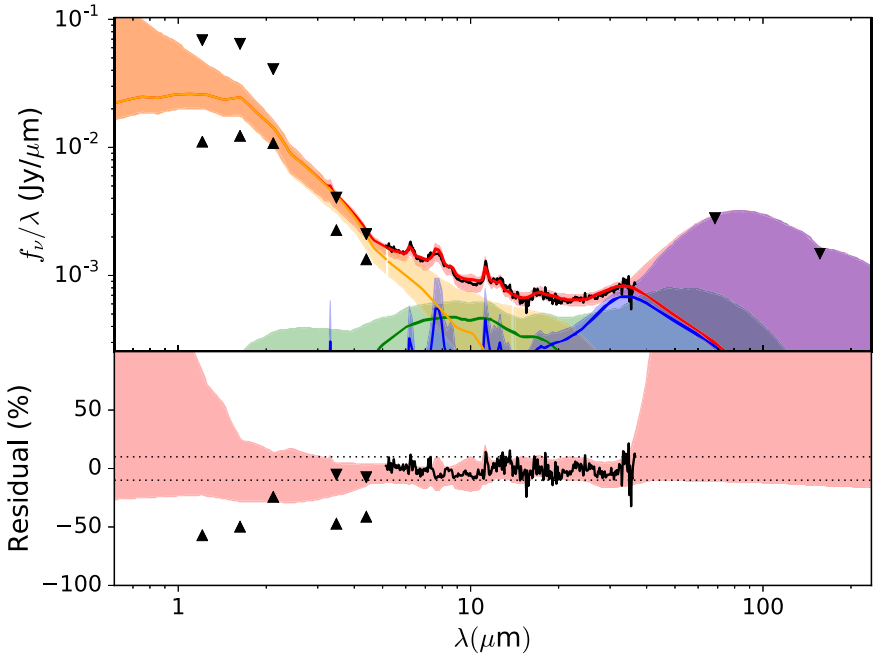

Figure 15. Continuum fit for NGC 3862 forcing a torus component (green). The model is otherwise the same as in Figure 14.

5.9. M87

We show our best fit for NGC 7052 in Figure 20, the best fit with a forced-torus component in Figure 21, and the fractional contributions to the flux in each of the two models in Tables 29 and 30, respectively. Although every source in our sample has a radio jet and a couple have large-scale optical jets, M87 is the only source in which the red power-law synchrotron spectrum of the inner jet provides a significant contribution to the IR flux. This power law has a best-fit index of $\alpha = 1.2$ (recall that we use the $L_\nu \propto \nu^{-\alpha}$ convention), which is consistent with the optical spectral indices of $\alpha_o \sim 1.0$–1.2 Perlman et al. (2001) found for interknot regions of the inner jet. The model with a "forced" torus component, shown in Figure 21, actually has a marginally lower BIC (392.0) than the otherwise "best" fit (398.7), shown in Figure 20, but this must be a fitting artifact, as it contributes no flux. This lack of a torus and strong power-law spectrum is consistent with findings by Whysong & Antonucci (2004), previously mentioned in Section 1.2, that M87 is weak in IR and that its nuclear IR emission is consistent with a synchrotron spectrum from the base of its jet. Similarly, the absence of a torus is consistent with the upper limits on MIR thermal emission established by Perlman et al. (2007).

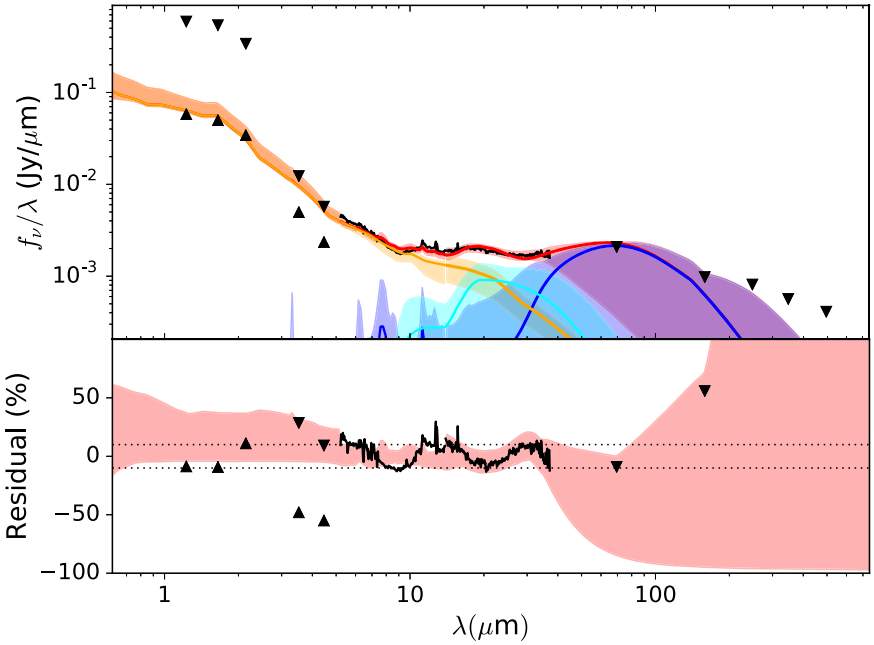

Figure 16. Best continuum fit for 3C 270. The model consists of a simple stellar population (yellow), NLR (cyan), and diffuse ISM (blue). The total fit is shown in red, although in the NIR it appears as orange owing to overlap with the stellar population. We have applied aperture correction between the SL and LL regions. Upright triangles represent lower limits from photometry, and inverted triangles represent upper limits.

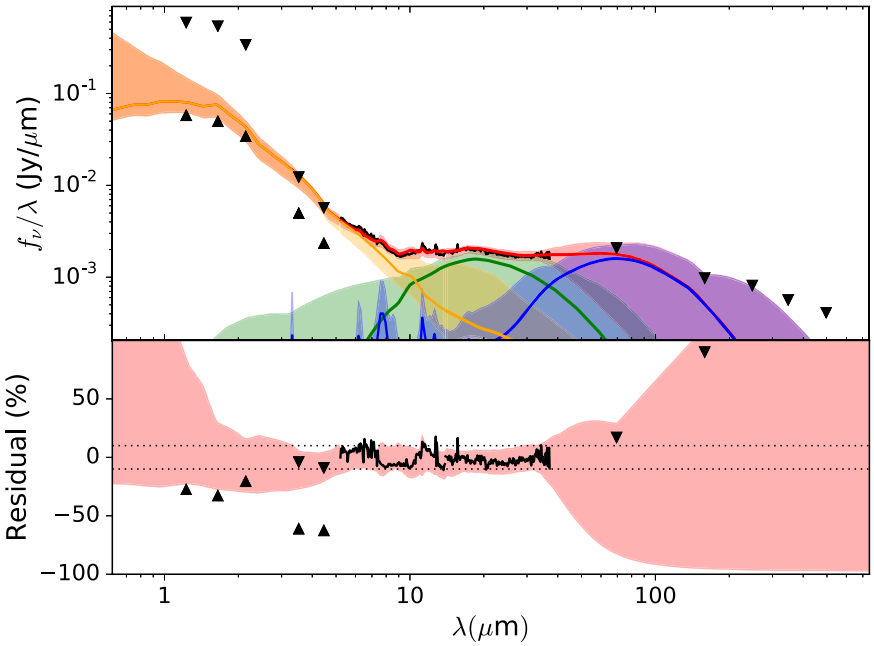

Figure 17. Continuum fit for 3C 270 forcing a torus component (green). To ensure maximal contribution from the torus component, we excluded the NLR component from Figure 16.

5.10. NGC 7052

We show our best fit for NGC 7052 in Figure 22, the best fit with a forced-torus component in Figure 23, and the fractional contributions to the flux in each of the two models in Tables 31 and 32, respectively. The model of NGC 7052 with the lowest BIC and the model with a forced torus have very similar goodness of fit, with the best fit having a BIC of 425.7 and the forced-torus fit having a BIC of 429.8. However, inspection of the forced-torus fit shows that it is unusually cold for a circumnuclear torus. Indeed, HST images of NGC 7052 by Verdoes Kleijn et al. (1999) show a promising candidate for such a cold thermal source in the form of a kiloparsec-scale dust disk that crosses the core region just off to the side of our line of sight into the nucleus. Overall, we conclude that a warm thermal component, such as a torus, is unnecessary to explain the IRS flux.

5.11. Continuum Fitting Summary

Some of the stellar age parameters for the best fits, shown in Table 33, are unusually low for the various SFR estimates. This

Table 26
Fractional Contributions of the Various Model Components to the Overall Continuum in 3C 270 with a Forced-torus Component

Component	Wavelength (μm)	Best Fit (%)	Minimum (%)	Maximum (%)
Torus	5.0	1.5	0.1	15.6
	15.0	73.6	10.6	86.7
	30.0	63.8	8.6	100.0
	60.0	13.0	1.6	44.0
Diffuse ISM	5.0	0.3	0.0	0.7
	15.0	6.5	0.9	13.9
	30.0	25.8	1.4	63.7
	60.0	84.0	4.5	100
Stars	5.0	98.2	75.7	100
	15.0	20.0	9.2	74.7
	30.0	10.4	1.3	30.7
	60.0	3.0	0.2	6.6

Table 27
Fractional Contributions of the Various Model Components to the Overall Continuum in the Best-fit Model for M84

Component	Wavelength (μm)	Best Fit (%)	Minimum (%)	Maximum (%)
Diffuse ISM	5.0	0.5	0.1	1.3
	15.0	19.9	8.8	35.7
	30.0	71.5	51.2	94.5
	60.0	99.3	40.3	100
Stars	5.0	37.6	27.4	77.4
	15.0	37.7	9.3	86.9
	30.0	11.3	1.8	35.0
	60.0	0.4	0.0	1.4
NLR	5.0	0.1	0.0	2.8
	15.0	13.2	0.0	27.6
	30.0	10.7	0.0	26.6
	60.0	0.2	0.0	8.4
Hot dust	5.0	61.8	17.0	73.1
	15.0	29.2	5.8	43.5
	30.0	6.6	1.2	10.7
	60.0	0.2	0.0	0.3

could be explained by those sources having recently quieted after a starburst; indeed, Das et al. (2005) claim something similar for NGC 3801, but it seems improbable that so many of such a small sample would be within 2 Gyr of the end of a starburst, and NGC 3801 is not one of the sources with these low stellar ages. The fits with a forced torus, shown in Table 34, are better in this regard, with only 3C 66B and M87 having this unusual combination. We do not put much stock in this result because stellar ages are generally poorly constrained by infrared data since young stars are brightest at shorter wavelengths and, as mentioned earlier, the GRASIL stellar population model assumes a single gigayear-long starburst followed by passive evolution, which may not be a good approximation in these galaxies. This would likely be clearer with more NIR spectrometry, and optical spectroscopy (especially in blue) would help characterize the population of young stars.

The diffuse ISM components of the two model sets, the best-fit models shown in Table 35 and the forced-torus models shown

Table 28
Fractional Contributions of the Various Model Components to the Overall Continuum in M84 with a Forced-torus Component

Component	Wavelength (μm)	Best Fit (%)	Minimum (%)	Maximum (%)
Torus	5.0	9.5	0.0	17.2
	15.0	33.6	0.0	67.4
	30.0	14.1	0.0	46.5
	60.0	0.2	0.0	3.0
Diffuse ISM	5.0	0.3	0.1	0.8
	15.0	16.0	7.0	21.4
	30.0	65.7	45.1	80.8
	60.0	98.9	46.1	100
Stars	5.0	90.2	82.5	100
	15.0	50.4	21.0	95.1
	30.0	20.3	3.7	46.6
	60.0	0.9	0.1	2.2

Table 29
Fractional Contributions of the Various Model Components to the Overall Continuum in the Best-fit Model of M87

Component	Wavelength (μm)	Best Fit (%)	Minimum (%)	Maximum (%)
Diffuse ISM	5.0	0.0	0.0	0.4
	15.0	1.3	0.0	8.2
	30.0	4.5	0.0	45.1
	60.0	26.1	0.0	89.5
Stars	5.0	90.3	41.5	98.4
	15.0	65.1	12.8	84.2
	30.0	36.4	7.2	46.5
	60.0	8.1	1.6	10.0

Table 30
Fractional Contributions of the Various Model Components to the Overall Continuum in M87 with a Forced-torus Component

Component	Wavelength (μm)	Best Fit (%)	Minimum (%)	Maximum (%)
Torus	5.0	0.0	0.0	1.0
	15.0	0.0	0.0	5.7
	30.0	0.2	0.0	31.8
	60.0	0.4	0.0	46.2
Diffuse ISM	5.0	0.0	0.0	0.4
	15.0	0.9	0.6	7.4
	30.0	3.2	2.0	23.4
	60.0	7.3	4.2	25.6
Stars	5.0	89.0	63.0	100
	15.0	64.4	37.8	83.3
	30.0	36.7	19.9	47.0
	60.0	10.3	4.8	12.9

in Table 36, show lower limits on their interstellar radiation fields, PAH fractions, and ISM luminosities, which are generally consistent between the two sets with the exception of M87, which shows an improbably weak radiation field and significantly higher ISM luminosity in the forced-torus model.

The fit parameters for the torus, when present (forced-torus models and NGC 315), are shown in Tables 37 and 38. Of

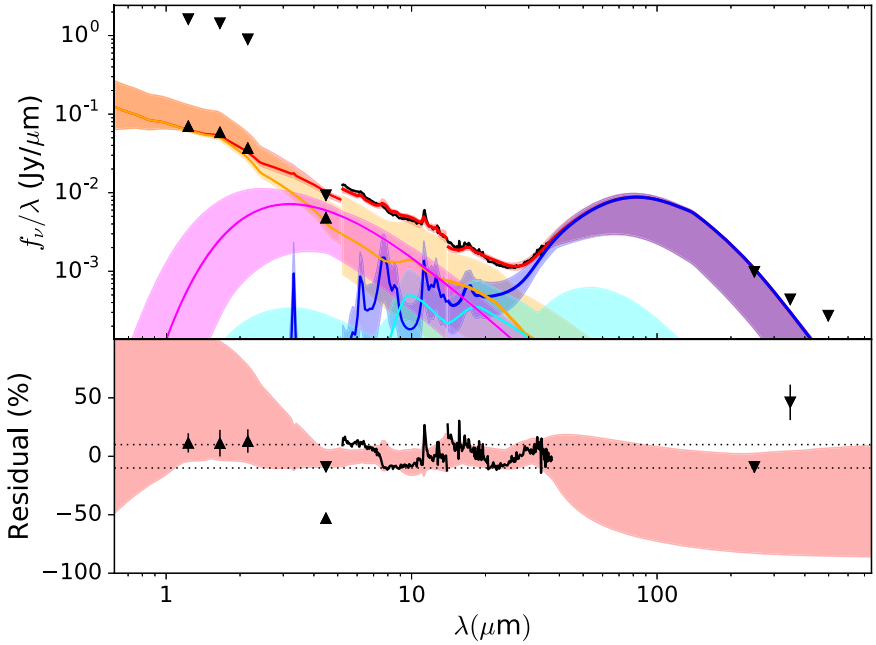

Figure 18. Best continuum fit for M84. The model consists of a simple stellar population (yellow), hot dust (pink), NLR (cyan), and diffuse ISM (blue). The total fit is shown in red, although in the NIR it appears as orange owing to overlap with the stellar population. We have applied aperture correction between the SL and LL regions, but this aperture correction was a fitting parameter and seems to have not been fit well. Upright triangles represent lower limits from photometry, and inverted triangles represent upper limits.

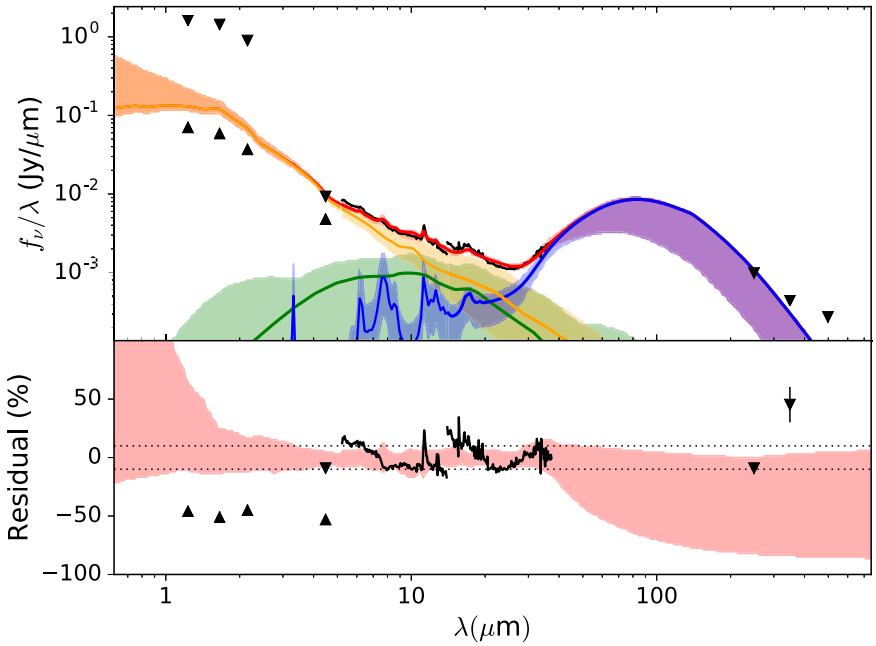

Figure 19. Continuum fit for M84 forcing a torus component (green). To ensure maximal torus component, we excluded the NLR and hot dust components seen in Figure 18.

particular interest is the low inclination of NGC 3801 and the large half-opening angle and high escape probability of NGC 3801, NGC 3862, and M84. These are unusual for sources in which we cannot see broad lines from the central engine. The masses of obscuring material in the forced-torus fits to NGC 3801 and M84 are remarkably small compared to the others, with both being $\sim 10^{-3}\,M_\odot$. And finally, the power-law indices of the cloud distributions in the forced-torus models are inconsistent with the silicate line ratios in several sources, especially three previously mentioned in this paragraph: NGC 3801, NGC 3862, and M84. When considered together, these issues suggest that the forced-torus fits to NGC 3801, NGC 3862, and M84 are inconsistent with independent observations.

Overall, we find no evidence for a warm obscuring torus in 6 of our 10 sources, and we find convincing evidence for a torus in 1 of the 10 (NGC 315). We have three more sources in which we find strong evidence for some warm MIR structure but cannot

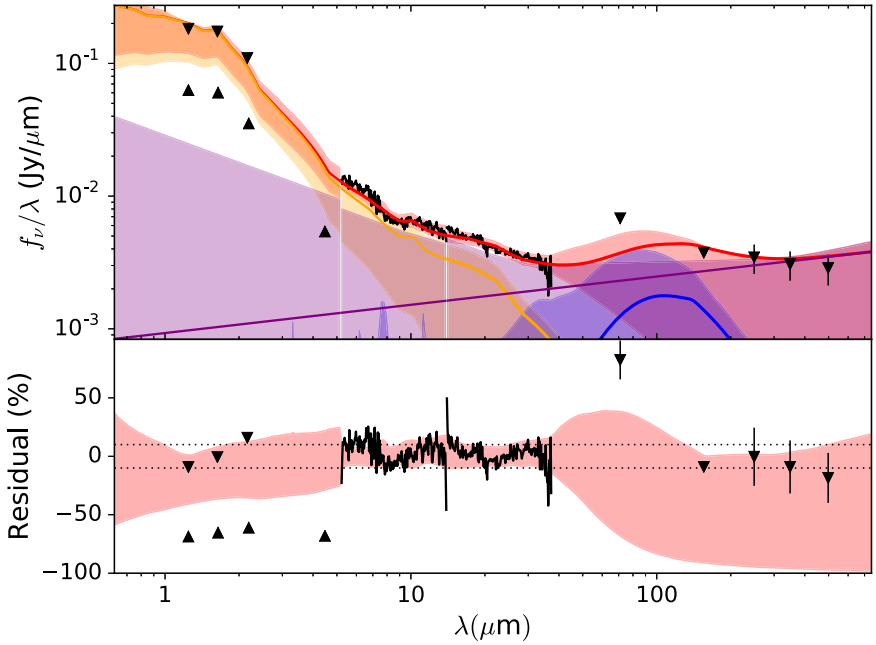

Figure 20. Best continuum fit for M87. The model consists of a power law (purple), a simple stellar population (yellow), and diffuse ISM (blue). The total fit is shown in red, although in the NIR it appears as orange owing to overlap with the stellar population. We have applied aperture correction between the SL and LL regions. Upright triangles represent lower limits from photometry, and inverted triangles represent upper limits.

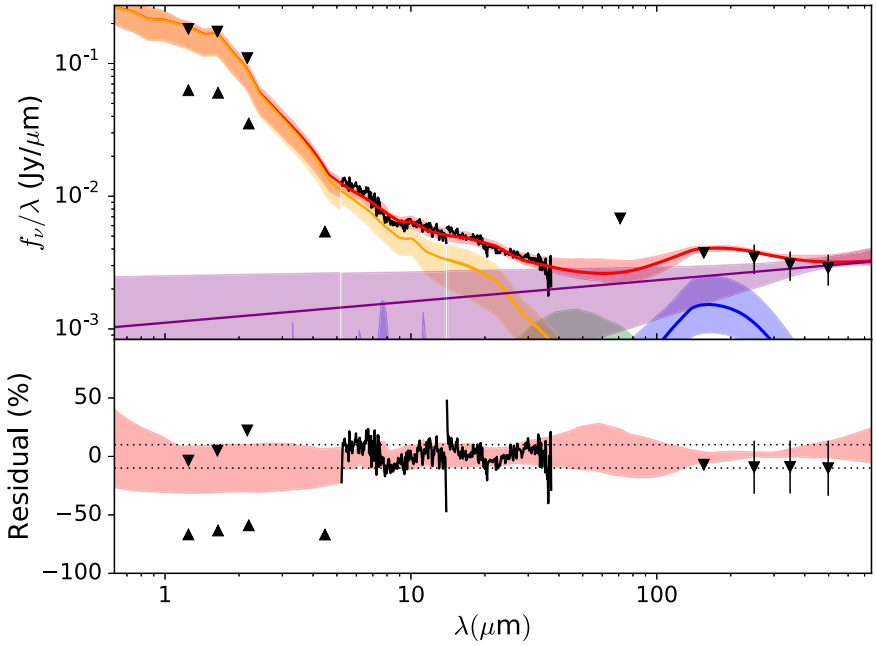

Figure 21. Continuum fit for M87 forcing a torus component (green). To ensure maximal torus component, we excluded the NLR component seen in Figure 20.

conclude that said structure is consistent with the Nenkova et al. (2002) clumpy torus model. We summarize our conclusions as to the presence or absence of each of our model components for each source in Table 39, and we compare the BIC of the best-fit models to those with a forced-torus component in Table 40. The main reason for inconclusive results is the fitting degeneracy between torus, NLR, and hot dust.

6. Discussion

Our results support the existence of a warm dusty structure in NGC 315, 3C 66B, 3C 270, and M84. Of those, only NGC 315 is clearly consistent with a clumpy obscuring torus. One more source, NGC 3801, benefits from the inclusion of a warm component. However, the best fit to the warm component in NGC 3801 is unusually dim relative to the ISM and stellar population compared to the other sources with a warm component.

A few of the sources in which we find no thermal component show significant silicate absorption, which may be due to larger-scale dust structures that would be too cool to appear in our continuum spectra. All of the thermal sources produce some silicate emission, as do two nonthermal sources. The silicate emission from nonthermal sources is harder to reconcile, though.

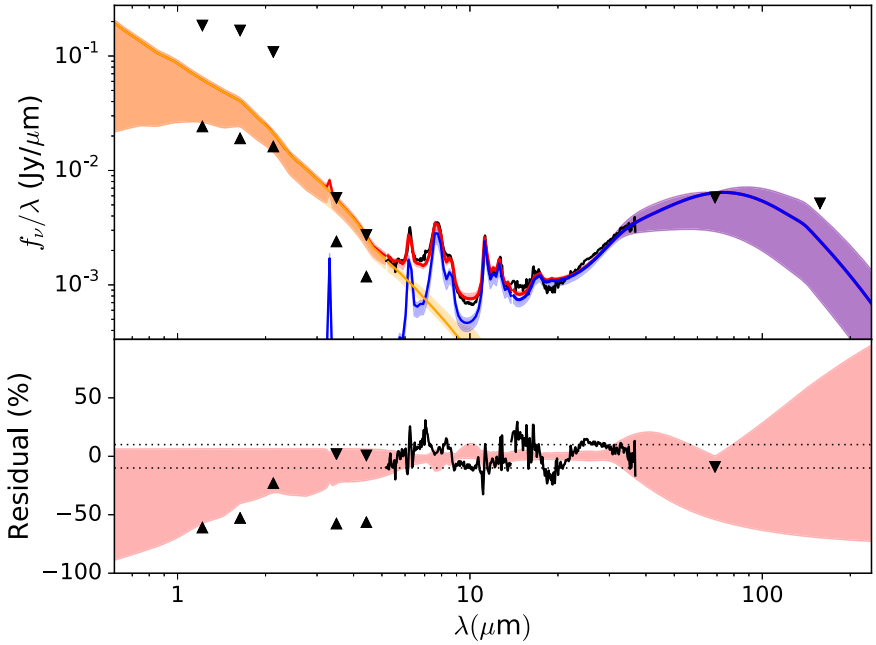

Figure 22. Best continuum fit for NGC 7052. The model consists of a simple stellar population (yellow) and diffuse ISM (blue). The total fit is shown in red, although in the NIR it appears as orange owing to overlap with the stellar population. Upright triangles represent lower limits from photometry, and inverted triangles represent upper limits.

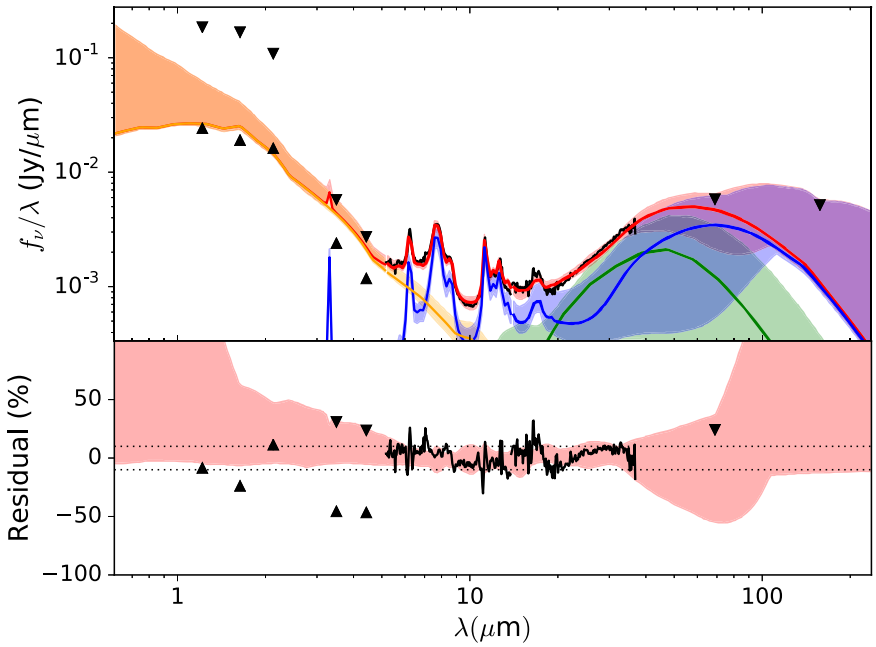

Figure 23. Continuum fit for NGC 7052 forcing a torus component (green). The model is otherwise the same as in Figure 23.

Perhaps those sources may be consistent with silicate emission from ADAF models or other nontorus possibilities that we have not explored because modeling those is beyond the scope of this paper.

We find that the thermal MIR excess Leipski et al. (2009) found in 3C 270 is better described by an NLR component. However, due to the bias in which the relative simplicity of the NLR component compared to the torus component biases the BIC against a torus component, this disagreement is quite minor. They also found an MIR excess in other sources in which we find a warm thermal component, 3C 66B and M84; however, they attribute these excesses to other effects, nonthermal emission in 3C 66B and starburst activity in M84. We rule out a starburst origin for the MIR excess in M84 because all our estimates of the SFR in M84 agree that SFR $\lesssim 0.1\,M_\odot$ (see Tables 11 and 33). Recall that Wu & Cao (2006) give an SFR estimate of $0.20\,M_\odot$ for M84, which is higher than our estimates but is still inconsistent with a starburst. Leipski et al. (2009) found a small MIR excess in 3C 31 as well, which they attribute to star formation. We do not find any of our thermal model components in 3C 31, but we believe that our SFRs listed in Tables 11 and 33 are

Table 31
Fractional Contributions of the Various Model Components to the Overall Continuum in the Best-fit Model for NGC 7052

Component	Wavelength (μm)	Best Fit (%)	Minimum (%)	Maximum (%)
Diffuse ISM	5.0	5.3	4.3	5.7
	15.0	90.8	79.3	92.6
	30.0	99.6	92.4	100
	60.0	100.0	50.8	100
Stars	5.0	94.7	77.6	100
	15.0	9.2	8.5	21.9
	30.0	0.4	0.4	3.9
	60.0	0.0	0.0	0.5

Table 32
Fractional Contributions of the Various Model Components to the Overall Continuum in NGC 7052 with a Forced-torus Component

Component	Wavelength (μm)	Best Fit (%)	Minimum (%)	Maximum (%)
Torus	5.0	3.9	0.0	9.5
	15.0	33.0	5.1	52.3
	30.0	60.9	14.8	92.4
	60.0	32.3	3.0	79.2
Diffuse ISM	5.0	5.3	4.1	6.3
	15.0	52.4	42.5	73.6
	30.0	35.8	14.6	83.8
	60.0	67.2	8.9	100
Stars	5.0	90.9	87.2	100
	15.0	14.6	7.2	26.1
	30.0	3.3	0.4	4.2
	60.0	0.5	0.0	0.6

Table 33
Best-fit Parameters for the Stellar Population Component

Source	Stellar Age (Gyr)	SFR ($M_\odot$ yr^{-1})
NGC 315	$7.7^{+3.0}_{-4.9}$	$0.24^{+0.15}_{-0.081}$
3C 31	$1.7^{+0.4}_{-0.7}$	$0.88^{+0.14}_{-0.28}$
NGC 541	$2.3^{+0.4}_{-0.4}$	$0.12^{+0.034}_{-0.017}$
3C 66B	$1.0^{+0.3}_{-0.2}$	$0.017^{+0.0038}_{-0.0035}$
NGC 3801	$9.4^{+3.0}_{-5.0}$	$0.35^{+0.087}_{-0.074}$
NGC 3862	$0.9^{+0.2}_{-0.3}$	$0.20^{+0.084}_{-0.038}$
3C 270	$1.0^{+0.2}_{-0.2}$	$0.044^{+0.0058}_{-0.014}$
M84	$0.4^{+0.1}_{-0.0}$	$0.034^{+0.0057}_{-0.0099}$
M87	$1.0^{+0.3}_{-0.2}$	$0.0026^{+0.0031}_{-0.0021}$
NGC 7052	$0.1^{+0.0}_{-0.0}$	$0.67^{+0.052}_{-0.061}$

Table 34
Best-fit Parameters for the Stellar Population Component in Fits Forcing a Torus

Source	Stellar Age (Gyr)	SFR ($M_\odot$ yr^{-1})
3C 31	7.9 ± 3.5	0.7 ± 0.2
NGC 541	$7.4^{+4.1}_{-3.6}$	$0.12^{+0.03}_{-0.01}$
3C 66B	$1.0^{+0.2}_{-0.2}$	$0.0005^{+0.0022}_{-0.0005}$
NGC 3801	$6.7^{+5.6}_{-6.4}$	$0.3^{+0.09}_{-0.04}$
NGC 3862	$2.5^{+6.8}_{-1.5}$	$0.21^{+0.08}_{-0.04}$
3C 270	$8.2^{+3.6}_{-3.8}$	0.03 ± 0.01
M84	$3.2^{+1.5}_{-0.9}$	$0.022^{+0.004}_{-0.003}$
M87	$1.1^{+0.2}_{-0.3}$	0.011 ± 0.001
NGC 7052	$9.8^{+2.2}_{-2.9}$	$0.47^{+0.10}_{-0.06}$

Table 35
ISM Component Best-fit Parameters

Source	$u_{\rm min}$	$q_{\rm PAH}$ (%)	ISM Luminosity (10^{41} erg s^{-1})
NGC 315	$8.^{+10.}_{-5.}$	$2.46^{+1.24}_{-0.9}$	$52.0^{+34.0}_{-18.0}$
3C 31	$3.^{+2.}_{-1.}$	$2.6^{+1.0}_{-0.3}$	200^{+30}_{-60}
NGC 541	11^{+6}_{-5}	$3.8^{+0.6}_{-0.8}$	$26.^{+8.}_{-4.}$
3C 66B	$6.^{+5.}_{-3.}$	$1.1^{+0.8}_{-0.4}$	3.8 ± 0.8
NGC 3801	$1.9^{+2.4}_{-0.8}$	$3.4^{+0.8}_{-0.6}$	80 ± 20
NGC 3862	$9.^{+10.}_{-6.}$	$3.5^{+0.7}_{-0.9}$	$44.^{+19.}_{-8.}$
3C 270	$15.^{+6.}_{-8.}$	$1.3^{+0.7}_{-0.4}$	$10.^{+1.}_{-3.}$
M84	$10.^{+8.}_{-3.}$	$1.6^{+0.6}_{-0.3}$	$8.^{+1.}_{-2.}$
M87	$15.^{+7.}_{-12.}$	$2. \pm 1.$	$0.6^{+0.7}_{-0.5}$
NGC 7052	$16.^{+5.}_{-4.}$	2.4 ± 0.2	150 ± 10

Note. Recall that $q_{\rm PAH}$ is the mass fraction of PAHs relative to the total dust mass and $U_{\rm min}$ is the lower limit of the interstellar radiation field as a scaling of that in the solar neighborhood.

Table 36
ISM Component Best-fit Parameters with a Forced-torus Component

Source	$u_{\rm min}$	$q_{\rm PAH}$ (%)	ISM Luminosity (10^{41} erg s^{-1})
3C 31	$3.^{+4.}_{-1.}$	$3.1^{+1.1}_{-0.6}$	$160 \pm +50$
NGC 541	$15.^{+4.}_{-8.}$	$4.0^{+0.4}_{-0.6}$	$26.^{+6.}_{-3.}$
3C 66B	$7.^{+7.}_{-4.}$	$2.^{+2.}_{-1.}$	$0.1^{+0.5}_{-0.1}$
NGC 3801	$4. \pm 2.$	$3.9^{+0.5}_{-0.8}$	$67.^{+19.}_{-9.}$
NGC 3862	$10.^{+9.}_{-6.}$	$3.5^{+0.7}_{-0.9}$	$46.^{+18.}_{-9.}$
3C 270	$14. \pm -8.$	$2.1^{+1.2}_{-0.9}$	$6.^{+3.}_{-2.}$
M84	$18.^{+4.}_{-5.}$	$1.3^{+0.4}_{-0.3}$	$4.9^{+1.0}_{-0.6}$
M87	$0.1^{+0.0}_{-0.0}$	$1.6^{+1.1}_{-0.8}$	2.5 ± 0.2
NGC 7052	$17.^{+4.}_{-8.}$	3.8 ± 0.6	100^{+20}_{-10}

sufficient to be loosely consistent with their results. Thus, the results of Leipski et al. (2009) seem consistent with our detection of a warm thermal component in 3C 270 and M84 but not 3C 66B, and our overall conclusion is similar to theirs despite some different conclusions regarding individual objects. We believe that our analysis is more effective at differentiating between different MIR and thermal model components than that performed by Leipski et al. (2009) because MCMC is known for its efficiency at exhaustive searches through large and complex parameter spaces (see Sales et al. 2015) but our more specific results rest on the validity of the Nenkova et al. (2008a, 2008b) torus models, which are not unique.

Since the luminosity of a given high-ionization line will be dependent on both the degree of ionization and the overall abundance of the element in question (see Spinoglio & Malkan 1992), we show the line ratio of our fitted [O IV] luminosities to archival [O III] luminosities for each of our sample galaxies in Table 41. This ratio is independent of the oxygen abundance in the line-emitting gas and as such provides a better indication of the ionization state of the gas at the cost of greater sensitivity to reddening than line rations with more

Table 37
Best-fit Parameters for Forced-torus Components

Source	σ (deg)	Y	N_0	τ_V	q	Inclination (deg)
NGC 315[a]	$60._{-10.}^{+8.}$	$21._{-7.}^{+25.}$	$12._{-3.}^{+2.}$	130_{-30}^{+50}	$1.3_{-0.9}^{+0.6}$	60 ± 20
3C 31	50_{-20}^{+10}	30_{-20}^{+40}	$11._{-4.}^{+3.}$	70_{-40}^{+120}	$1.9_{-1.0}^{+0.6}$	50 ± 30
NGC 541	50_{-20}^{+10}	40_{-20}^{+40}	$10._{-4.}^{+3.}$	150_{-90}^{+100}	$1.7_{-1.0}^{+0.8}$	50_{-30}^{+20}
3C 66B	60 ± 10	$24._{-6.}^{+22.}$	$11._{-4.}^{+3.}$	220_{-70}^{+50}	$1.00_{-0.68}^{+0.70}$	70_{-20}^{+10}
NGC 3801	40 ± 20	50_{-30}^{+40}	$4._{-2.}^{+5.}$	30_{-10}^{+140}	$2.4_{-1.1}^{+0.5}$	30_{-20}^{+30}
NGC 3862	40 ± 20	50_{-30}^{+40}	$7._{-4.}^{+5.}$	100_{-70}^{+120}	$2.2_{-1.2}^{+0.5}$	40 ± 30
3C 270	$58._{-13.}^{+8.}$	$16._{-5.}^{+36.}$	$12._{-3.}^{+2.}$	140_{-40}^{+80}	$1.6_{-1.0}^{+0.7}$	60_{-30}^{+20}
M84	40 ± 20	30_{-20}^{+40}	$7._{-4.}^{+5.}$	40_{-30}^{+120}	$2.5_{-0.7}^{+0.4}$	40 ± 30
M87	60_{-20}^{+10}	80 ± 20	$11._{-4.}^{+2.}$	200 ± 70	$0.5_{-0.3}^{+0.4}$	70_{-30}^{+20}
NGC 7052	$64._{-7.}^{+4.}$	$90._{-10.}^{+7.}$	$12. \pm 2.$	60 ± 20	$0.3_{-0.2}^{+0.3}$	60_{-20}^{+20}

Notes. σ is the angular scale height of the torus, Y is the radial extent of the torus in units of the dust sublimation radius, N_0 is the number of clouds along an equatorial line of sight, τ_V is the optical depth of a single cloud, and q is the power-law index of the radial distribution of clouds. The inclination is defined such that 0° is pole-on and 90° is edge-on.
[a] Recall that NGC 315 favors a torus component; it is not forced.

Table 38
More Best-fit Parameters for Forced-torus Components

Source	Half-Opening Angle (deg)	Escape Probability (%)	Mass ($M_\odot$)	Radius (pc)	AGN Luminosity (10^{41} erg s^{-1})
NGC 315[a]	$10._{-3.}^{+6.}$	$0.02_{-0.0}^{+0.60}$	$2.2_{-0.9}^{+1.4}$	$0.9_{-0.3}^{+1.2}$	110_{-20}^{+30}
3C 31	$15._{-6.}^{+16.}$	$0.8_{-0.7}^{+24.5}$	$0.04_{-0.03}^{+0.09}$	$0.4_{-0.3}^{+0.5}$	$9._{-3.}^{+5.}$
NGC 541	$18._{-9.}^{+21.}$	$1._{-1.}^{+40.}$	$0.04_{-0.03}^{+0.11}$	$0.3_{-0.2}^{+0.4}$	$4._{-2.}^{+3.}$
3C 66B	$13._{-5.}^{+10.}$	$0.02_{-0.0}^{+0.55}$	$0.4_{-0.2}^{+0.3}$	$0.31_{-0.09}^{+0.27}$	$9._{-2.}^{+3.}$
NGC 3801	40 ± 20	70_{-50}^{+30}	$0.001_{-0.001}^{+0.005}$	$0.3_{-0.2}^{+0.4}$	$4. \pm 3.$
NGC 3862	40 ± 20	30_{-30}^{+70}	$0.03_{-0.02}^{+0.11}$	$0.6_{-0.5}^{+0.9}$	20 ± 20
3C 270	$11._{-3.}^{+8.}$	$0.03_{-0.00}^{+1.37}$	$0.09_{-0.04}^{+0.06}$	$0.19_{-0.08}^{+0.47}$	$9._{-2.}^{+3.}$
M84	30 ± 20	20_{-20}^{+80}	$0.0008_{-0.0005}^{+0.0012}$	$0.13_{-0.09}^{+0.21}$	$1.2_{-0.6}^{+0.8}$
M87	$13._{-4.}^{+16.}$	$0.04_{-0.00}^{+1.44}$	$0.1_{-0.1}^{+0.3}$	0.1 ± 0.1	$0.2_{-0.2}^{+0.6}$
NGC 7052	$8._{-1.}^{+2.}$	$0.02_{-0.00}^{+0.15}$	$14._{-5.}^{+9.}$	2.3 ± 0.3	$41._{-7.}^{+8.}$

Note.
[a] Recall that NGC 315 favors a torus component; it is not forced.

Table 39
Summary of Best-fit Results

Source	Evidence for Torus	Evidence for Power Law	Evidence for NLR	Evidence for Hot Dust	Warm Component?
NGC 315	Y	N	N	N	Y
3C 31	N	N[a]	N	N	N
NGC 541	N	N	N	N	N
3C 66B	I	N[a]	I	I	Y
NGC 3801	N	N	I	N	I
NGC 3862	N	N[a]	N	N	N
3C 270	I/Y	N	I/N	N	Y
M84	I	N	I	I	Y
M87	N	Y[a]	N	N	N
NGC 7052	N	N	N	N	N

Notes. Results in which we are reasonably confident are marked with "Y" (for yes) if present or "N" (for no) if not. Results that are more ambiguous are denoted with "I" (for inconclusive), although we follow the 3C 270 results with a marker describing the model that we favor. The NLR and torus are both considered a warm component.
[a] These sources have known optical or IR jets and so were checked for a power-law component.

Table 40
BIC for the the Best Fit and Forced-torus Fit in Each Source

Source	Best-fit BIC	Forced-torus BIC
NGC 315	420.3	⋯
3C 31	403.5	425.7
NGC 541	380.5	408.7
3C 66B	472.3	506.8
NGC 3801	423.5	453.7
NGC 3862	391.9	420.3
3C 270	410.7	424.9
M84	386.9	444.4
M87	398.7	392.0
NGC 7052	425.7	429.8

Note. Recall that we do not favor the presence of a torus in M87 despite the lower BIC because the torus component does not contribute to the flux when forced.

Table 41
Oxygen Line Ratios in Our Sample of FR I Sources

Source	$L_{[\mathrm{O\,IV}]}$ 26 μm (10^{39} erg s^{-1})	$L_{[\mathrm{OIII}]}$ (10^{39} erg s^{-1})	$\frac{L_{[\mathrm{O\,IV}]}}{L_{[\mathrm{O\,III}]}}$	[O III] Reference
NGC 315	<4.98	2.75	<1.81	Balmaverde et al. (2016)
3C 31	$3.5^{+0.7}_{-0.8}$	2.88	$1.2^{+0.2}_{-0.3}$	Buttiglione et al. (2010)
NGC 541	<6.28	0.886	<7.09	Constantin et al. (2015)
3C 66B	<3.10	11.2	<0.28	Buttiglione et al. (2010)
NGC 3801	<3.20	0.146	<22.0	Sikora et al. (2013)
NGC 3862	<4.12	1.58	<2.60	Buttiglione et al. (2010)
3C 270	<0.924	0.794	<1.16	van der Wolk et al. (2010)
M84[a]	$0.32^{+0.04}_{-0.06}$	0.88	$0.36^{+0.04}_{-0.07}$	Richings et al. (2011)
M87	<0.751	1.17	<0.64	Balmaverde et al. (2016)
NGC 7052	<7.60	2.75	<2.76	Baldi & Capetti (2009)

Note.
[a] Richings et al. (2011) uses a different cosmology from ours, so we have corrected their $L_{[\mathrm{O\,III}]}$ to our distance.

similar wavelengths, e.g., Hβ/[O III]. However, most of the ratios for our sample are upper limits because no [O IV] was detected in those sources. The two FR I sources in which we detected [O IV] emission are inconsistent with broad-line radio galaxies and quasars in the Haas et al. (2005) sample and consistent with obscured sources (e.g., Seyfert 2) in the Baum et al. (2010) Seyfert sample.

To put together all our lines of evidence, we summarize in Table 42 all our results and those we found in the literature. We note that most sources that show at least one test with an inconclusive or positive result also show inconclusive or positive results on other tests. In particular, all sources that show evidence of a warm component are backed up by at least one additional line of evidence.

Recall the suggestion by Elitzur & Shlosman (2006) that hydromagnetic disk winds off sources with bolometric luminosities $L_{\mathrm{bol}} \lesssim 10^{42}$ erg s^{-1} could not sustain a clumpy obscuring torus. In the torus model parameter continuum fits with a forced-torus component, shown in Table 38, NGC 315, NGC 3862, and NGC 7052 have best-fit AGN luminosities $>10^{42}$ erg s^{-1} and 3C 31, 3C 66B, and 3C 270 come in just under that at $\sim 9 \times 10^{41}$ erg s^{-1}. If Elitzur & Shlosman (2006) are correct, this suggests that the other four sources, which all have bolometric luminosities significantly below 10^{42} erg s^{-1},

Table 42
Summary of Evidence for a Warm Obscuring Structure in Each Source

Source	Warm Component (Ours)	Warm Component (Others)	Broad Polarized Hα	High [O IV]/[O III]
NGC 315	Y	⋯	Y	N
3C 31	N	N	Y	Y
NGC 541	N	⋯	N	N
3C 66B	Y	I	Y	N
NGC 3801	I	⋯	N	N
NGC 3862	N	N	N	N
3C 270	Y	Y	I	N
M84	Y	Y	N	Y
M87	N	N	N	N
NGC 7052	N	⋯	N	N

Note. "Others" includes classifications by Leipski et al. (2009), except for M87; classification for M87 by Whysong & Antonucci (2004) and Perlman et al. (2007). Broad polarized Hα references: NGC 315 (Barth et al. 1999); 3C 31 (Constantin et al. 2015); 3C 66B (Constantin et al. 2015); 3C 270 (R. Antonucci, private communication). "Y" (for "yes") denotes that the evidence from this method supports the presence of a warm obscuring structure, "N" denotes that it does not, "I" denotes that the evidence isn't conclusive either way.

Table 43
Classification Based on Excitation Indices

Source	$L_{H\alpha}$	$L_{H\beta}$	$L_{[N\ II]}$	$L_{[S\ II]}$	$L_{[O\ I]}$	EI	Class
NGC 315[a]	4.19	4.80	7.70	2.12	2.46	−0.154	ELERG
3C 31	6.76	1.01	6.69	4.66	0.946	0.797	LERG
NGC 541	4.58	1.32	2.97	0.57	1.10	−0.484	ELERG
3C 66B	12.88	1.54	31.16	7.21	3.35	0.746	LERG
NGC 3801	0.98	0.06	0.96	0.57	0.17	0.721	LERG
NGC 3862	4.79	1.29	6.94	3.16	1.05	0.313	LERG
3C 270[b]	0.14	<0.15	0.10	<0.12	0.07	0.048	LERG
M84	0.83	0.08	1.06	0.72	0.19	0.478	LERG
M87	3.16	0.54	7.34	4.58	1.14	0.233	LERG
NGC 7052	7.62	1.65	8.86	3.62	0.93	0.612	LERG

Notes. All luminosities in units of 10^{39} erg s^{-1}. $L_{[O\ III]}$ given in Table 41. Line luminosities and excitation indices for galaxies in 3C (3C 31, 3C 66B, NGC 3862, 3C 270, M84, and M87) by Hu et al. (2016). Line luminosities for NGC 541, NGC 3801, and NGC 7052 by Constantin et al. (2015). Hα and [O I] line luminosities for NGC 315 by Cid Fernandes et al. (2004), Hβ by Richings et al. (2011), and [N II] and [S II] by Balmaverde et al. (2016). Classification cutoff given by Buttiglione et al. (2010) as EI $\lesssim$ 0.95 for low-excitation galaxies. Hu et al. (2016) calculated EI using line fluxes by Buttiglione et al. (2009).
[a] Cid Fernandes et al. (2004) and Richings et al. (2011) use a different cosmology than us, so we have corrected their luminosities for our distance. Additionally, since the luminosities are from different instruments, systematic errors in our calculations are likely significant and difficult to quantify.
[b] Buttiglione et al. (2010) removed this source from their data owing to a misplaced SDSS fiber. We have included it for completeness, but it is unreliable.

including M84, which we previously considered inconclusive, are not likely to host a clumpy AGN-wind-driven torus. Note, however, that this does not necessarily prohibit other obscuring structures.

Buttiglione et al. (2010) proposed various line ratios with which to distinguish between low-excitation and high-excitation sources. The measure with the clearest distinction between the two populations was the Excitation Index (EI), defined as

$$\mathrm{EI} = \log\frac{[\mathrm{O\ III}]}{\mathrm{H}\beta} - \frac{1}{3}\left(\log\frac{[\mathrm{N\ II}]}{\mathrm{H}\alpha} + \log\frac{[\mathrm{S\ II}]}{\mathrm{H}\alpha} + \log\frac{[\mathrm{O\ I}]}{\mathrm{H}\alpha}\right). \quad (9)$$

For low-excitation sources EI $\lesssim$ 0.95, and for high-excitation sources EI $\gtrsim$ 0.95. Hu et al. (2016) calculated excitation indices for the 3C catalog using line fluxes measured by Buttiglione et al. (2009), and we include those 3C sources that are also in our sample in Table 43 and find that all but NGC 315 and NGC 541 are low-excitation sources. We classify those remaining two as extremely low excitation radio galaxies (ELERGs) based on their unusually low [O III]/Hβ of 0.57 and 0.67, respectively, which is consistent with the [O III]/H$\beta \sim 0.5$ indicative of extremely low excitation sources. Capetti et al. (2011) describe extremely low excitation galaxies as "radio relics," i.e., sources that recently experienced a drop in nuclear activity—perhaps this is the case in NGC 315 and NGC 541. We see no issues with this interpretation for NGC 541, but NGC 315 shows a warm thermal MIR component. This warm thermal component in NGC 315 is well fit by a clumpy torus and is thus indicative of a high-excitation galaxy, yet its optical emission-line ratios are those of an extremely low excitation galaxy. We hypothesize that the warm dust cooling is occurring on a longer timescale than [O III] recombination, perhaps because the warm dust structure is much larger than the emission-line nucleus.

We compare our continuum fitting results to 1.4 GHz radio luminosity density $L_{\nu,1.4\mathrm{GHz}}$, estimated black hole mass M_{BH}, Eddington luminosity L_{Edd}, and core-extended brightness ratio R_c in Table 44. R_c is an indicator for AGN orientation based on relativistic beaming of the radio jet (Orr & Browne 1982; Zirbel & Baum 1995). The presence or absence of an MIR thermal component appears to be independent of $L_{\nu,1.4\mathrm{GHz}}$, R_c, and redshift, but there may be some dependence on black hole mass. No source in the sample with an estimated black hole mass below $7 \times 10^8\,M_\odot$ has an MIR thermal component, and only two sources (3C 31 and M87) without an MIR thermal component have black hole masses above that. However, this should be viewed with caution owing to the small sample size.

We also compare the best-fit AGN bolometric luminosity output by the forced-torus clumpyDREAM runs (and NGC 315; see Table 38) to bolometric luminosity estimates based on archival [O III] luminosities (see Table 41) using a

Table 44
Similar to Table 2, We Show the 1.4 GHz Radio Luminosity Density, Black Hole Mass Estimate, Eddington Luminosity, and Logarithm of Core-extended Brightness Ratio (an Indicator for AGN Orientation) for FR I AGNs in Our Sample

Source	$L_{\nu,1.4\mathrm{GHz}}$ (10^{31} erg s^{-1} Hz^{-1})	M_{BH} ($10^8\,M_\odot$)	L_{Edd} (10^{47} erg s^{-1})	$\log_{10}R_c$
NGC 315	1.26	14.6	1.84	−0.39
3C 66B	8.71	18.6	2.34	−1.29
M84	0.224	7.30	0.920	−1.18
3C 270	2.51	7.75	0.976	−1.44
3C 31	3.24	9.24	1.16	−1.34
NGC 541	0.871	2.03	0.226	⋯
NGC 3801	0.309	1.53	0.193	⋯
NGC 3862	5.62	4.66	0.587	−1.00
M87	7.94	22.5	2.84	−1.24
NGC 7052	0.110	3.62	0.456	−0.22

Note. Here we have divided the sample based on the presence (top) or absence (bottom) of an MIR thermal component in the best fit for each source. $L_{\nu,1.4\mathrm{GHz}}$ by Condon & Broderick (1988), M_{BH} by Noel-Storr et al. (2007) based on a relation by Merritt & Ferrarese (2001), and $\log_{10}R_c$ by Kharb & Shastri (2004). We notice no dependence of the presence of a thermal MIR component on $L_{\nu,1.4\mathrm{GHz}}$, R_c, or redshift (see Table 1). Sources with a thermal MIR component seem to have larger M_{BH} as a group; however, 3C 31 and M87 do not fit with that distinction, and we can think of no clear reason why this should be the case.

Table 45
Comparison of Bolometric Luminosity Estimate from [O III] Emission L_{bol} (see Table 41) to the Best-fit Luminosity from Forced-torus clumpyDREAM Runs (see Table 38)

Source	$L_{[O\ III]}$ (10^{39} erg s^{-1})	L_{bol} (10^{41} erg s^{-1})	L_{clumpy} (10^{41} erg s^{-1})	$\frac{L_{clumpy}}{L_{bol}}$
NGC 315[a]	2.75	96.3 ± 84.2	$110.0^{34.0}_{21.0}$	$1.14^{1.35}_{1.14}$
3C 31	2.88	101 ± 88.2	$9.1^{4.9}_{2.8}$	$0.090^{0.13}_{0.11}$
NGC 541	0.886	31.0 ± 27.1	$4.5^{2.8}_{1.5}$	$0.15^{0.22}_{0.18}$
3C 66B	11.2	392 ± 343	$9.1^{3.3}_{1.6}$	$0.023^{0.029}_{0.024}$
NGC 3801	0.146	5.11 ± 4.47	$4.0^{3.2}_{2.7}$	$0.78^{1.31}_{1.21}$
NGC 3862	1.58	55.3 ± 48.4	$20.0^{20.0}_{18.0}$	$0.36^{0.68}_{0.64}$
3C 270	0.794	27.8 ± 24.3	$9.0^{2.9}_{1.8}$	$0.32^{0.39}_{0.35}$
M84	0.88	30.8 ± 27.0	$1.2^{0.8}_{0.6}$	$0.039^{0.061}_{0.052}$
M87	1.17	41.0 ± 35.8	$0.21^{0.58}_{0.20}$	$0.0051^{0.019}_{0.0094}$
NGC 7052	2.75	96.3 ± 84.2	$41.0^{8.2}_{6.6}$	$0.4^{0.5}_{0.4}$

Note.
[a] Recall that the best fit to NGC 315 includes a torus component.

Table 46
Estimated Eddington Ratios for Each Source Based on the Noel-Storr et al. (2007) Black Hole Mass Estimates Listed in Table 44 and the Bolometric Luminosity Estimates Listed in Table 45

Source	$\log_{10}\left(\frac{L_{clumpy}}{L_{Edd}}\right)$	$\log_{10}\left(\frac{L_{bol}}{L_{Edd}}\right)$
NGC 315	−4.22	−4.28
3C 31	−5.10	−4.06
NGC 541	−4.70	−3.86
3C 66B	−5.41	−3.77
NGC 3801	−4.68	−4.58
NGC 3862	−4.47	−4.02
3C 270	−5.04	−4.54
M84	−5.88	−4.48
M87	−7.13	−4.84
NGC 7052	−4.05	−3.68

Note. We do not see a clear distinction between sources with a best-fit warm thermal component and those without.

calibration of

$$\frac{L_{bol}}{L_{[O\ III]}} = 3500 \pm 0.38 \text{ dex} \quad (10)$$

by Heckman et al. (2004). This calibration was developed for type 1 AGNs, so L_{bol} is likely to be underestimated in type 2 AGNs due to [O III] extinction by dust. We show the comparison in Table 45 and note that we only find $L_{clumpy}/L_{bol} \gtrsim 1$ in NGC 315. Even considering the large uncertainties on the bolometric luminosity estimate from [O III] emission, only NGC 315, NGC 3801, and NGC 3862 are consistent with $L_{clumpy} = L_{bol}$, assuming that the Heckman et al. (2004) calibration holds. This is consistent with our finding that NGC 315 has the best fit of a clumpy torus to its continuum infrared spectral energy distribution. All sources except NGC 315 have lower emission in the IR than would be expected given their [O III] luminosity. This is consistent with a lack of dusty circumnuclear gas in these LERG FR I galaxies. Dicken et al. (2010) note that low-redshift broad-line radio galaxies show enhanced [O III] emission and warmer MIR and far-infrared colors than narrow-line radio galaxies at similar redshift, but that compares broad-line objects to hidden broad-line objects and therefore says little about narrow-line objects without a hidden broad-line region.

In Table 46 we show estimates of the Eddington ration using black hole mass estimates by Noel-Storr et al. (2007) and our two bolometric luminosity estimates. All of these sources are extremely sub-Eddington with ratios of $<10^{-3.5}$. We do not see a clear distinction between sources with warm thermal components in their best clumpyDREAM fits and those without. This suggests that Eddington ratio is not the driving factor separating the two modes.

7. Conclusion

We used fitting codes based on MCMC algorithms to examine the IR spectra, primarily from Spitzer/IRS, of 10 nearby FR I radio galaxies (NGC 315, 3C 31, NGC 541, 3C 66B, NGC 3801, NGC 3862, 3C 270, M84, M87, and NGC 7052) in order to determine whether there is significant contribution in the MIR from warm dust. This dust would serve to obscure the central engine and thus explain why AGNs with high radio luminosities can resemble quiescent galaxies in optical wavelengths. The leading alternative model for an FR I is powered by an ADAF that puts the vast majority of its output power into a radio jet.

We see evidence for the IR signature of a warm dusty structure in only 4 of these 10 LERGs. The fact that we do not see evidence for a clumpy torus in six of the LERGs suggests not only that the central engine is different at these low luminosities (e.g., an ADAF) but also that the circumnuclear absorbing material is different from that in high-excitation sources. This difference in nuclear environment is consistent with previous results obtained using different methods (e.g., Capetti et al. 2005; Leipski et al. 2009; van der Wolk et al. 2010). All sources except NGC 315 have lower emission in the IR than would be expected given the observed [O III] luminosity using the calibration of Heckman et al. (2004). This is also consistent with a lack of dusty circumnuclear gas. The accretion rates onto the central black holes in LERGs are thought to be much less than those in the high-excitation sources (e.g., Baum et al. 1995; Hardcastle et al. 2009; Buttiglione et al. 2010; Best & Heckman 2012). The difference in circumnuclear environment is thought to be related to the

much lower accretion rates in the LERGs. Our Eddington ratio estimates do not support this, as they are all quite low, including the one in which we find evidence of an obscuring torus and all the ones where we found some thermal component.

However, four of the LERGs (NGC 315, 3C 66B, 3C 270, and M84) have infrared spectral energy distributions consistent with the presence of a significant amount of warm dust (one of which is consistent with a Nenkova et al. 2008a, 2008b clumpy torus), and three of the four (NGC 315, 3C 66B, 3C 270) show evidence for polarized Hα emission consistent with a hidden type 1 nucleus. This is puzzling. Perhaps these are objects in transition, possibly with either growing or declining accretion rate or possibly in a semistable intermediate state in a more complex transition. In any case, this suggests that the central engines in LERGs are not yet understood and that further work is needed.

This research has made use of the NASA/IPAC Extragalactic Database (NED), which is operated by the Jet Propulsion Laboratory, California Institute of Technology, under contract with the National Aeronautics and Space Administration. This publication makes use of data products from the Two Micron All Sky Survey, which is a joint project of the University of Massachusetts and the Infrared Processing and Analysis Center/California Institute of Technology, funded by the National Aeronautics and Space Administration and the National Science Foundation.

S.B. and C.O. acknowledge support from the Natural Sciences and Engineering Research Council of Canada (NSERC).

This work is based in part on observations made with the Spitzer Space Telescope, which is operated by the Jet Propulsion Laboratory, California Institute of Technology, under a contract with NASA.

SPIRE has been developed by a consortium of institutes led by Cardiff University (UK) and including Univ. Lethbridge (Canada); NAOC (China); CEA, LAM (France); IFSI, Univ. Padua (Italy); IAC (Spain); Stockholm Observatory (Sweden); Imperial College London, RAL, UCL-MSSL, UKATC, Univ. Sussex (UK); and Caltech, JPL, NHSC, Univ. Colorado (USA). This development has been supported by national funding agencies: CSA (Canada); NAOC (China); CEA, CNES, CNRS (France); ASI (Italy); MCINN (Spain); SNSB (Sweden); STFC, UKSA (UK); and NASA (USA).

Herschel is an ESA space observatory with science instruments provided by European-led Principal Investigator consortia and with important participation from NASA.

ORCID iDs

R. C. Gleisinger https://orcid.org/0000-0001-7935-7595
C. P. O'Dea https://orcid.org/0000-0001-6421-054X
J. F. Gallimore https://orcid.org/0000-0002-6972-2760
S. A. Baum https://orcid.org/0000-0002-4735-8224

References

Anderson, J. M., & Ulvestad, J. S. 2005, ApJ, 627, 674
Antonucci, R. 1993, ARA&A, 31, 473
Antonucci, R. 2012, A&AT, 27, 557
Astropy Collaboration, Robitaille, T. P., Tollerud, E. J., et al. 2013, A&A, 558, A33
Baes, M., Clemens, M., Xilouris, E. M., et al. 2010, A&A, 518, L53
Baldi, R. D., & Capetti, A. 2009, A&A, 508, 603
Balmaverde, B., Capetti, A., Moisio, D., Baldi, R. D., & Marconi, A. 2016, A&A, 586, A48
Barth, A. J., Filippenko, A. V., & Moran, E. C. 1999, ApJ, 525, 673
Baum, S. A., Gallimore, J. F., O'Dea, C. P., et al. 2010, ApJ, 710, 289
Baum, S. A., Zirbel, E. L., & O'Dea, C. P. 1995, ApJ, 451, 88
Best, P. N., & Heckman, T. M. 2012, MNRAS, 421, 1569
Bianchi, S., Antonucci, R., Capetti, A., et al. 2019, MNRAS, 488, L1
Blanton, M. R., Bershady, M. A., Abolfathi, B., et al. 2017, AJ, 154, 28
Bogdán, Á, Kraft, R. P., Forman, W. R., et al. 2011, ApJ, 743, 59
Bridle, A. H., & Vallee, J. P. 1981, AJ, 86, 1165
Butcher, H. R., van Breugel, W., & Miley, G. K. 1980, ApJ, 235, 749
Buttiglione, S., Capetti, A., Celotti, A., et al. 2009, A&A, 495, 1033
Buttiglione, S., Capetti, A., Celotti, A., et al. 2010, A&A, 509, A6
Capetti, A., Buttiglione, S., Axon, D. J., et al. 2011, A&A, 527, L2
Capetti, A., Verdoes Kleijn, G., & Chiaberge, M. 2005, A&A, 439, 935
Chiaberge, M., Capetti, A., & Celotti, A. 1999, A&A, 349, 77
Cid Fernandes, R., González Delgado, R. M., Schmitt, H., et al. 2004, ApJ, 605, 105
Condon, J. J., & Broderick, J. J. 1985, AJ, 90, 2540
Condon, J. J., & Broderick, J. J. 1986, AJ, 91, 1051
Condon, J. J., & Broderick, J. J. 1988, AJ, 96, 30
Constantin, A., Shields, J. C., Ho, L. C., et al. 2015, ApJ, 814, 149
Crane, P., Peletier, R., Baxter, D., et al. 1993, ApJL, 402, L37
Croston, J. H., Birkinshaw, M., Conway, E., & Davies, R. L. 2003, MNRAS, 339, 82
Cutri, R. M., Skrutskie, M. F., van Dyk, S., et al. 2003, 2MASS All Sky Catalog of Point Sources (Pasadena, CA: Cal Tech)
Das, M., Vogel, S. N., Verdoes Kleijn, G. A., O'Dea, C. P., & Baum, S. A. 2005, ApJ, 629, 757
Dicken, D., Tadhunter, C., Axon, D., et al. 2010, ApJ, 722, 1333
Donahue, M., de Messières, G. E., O'Connell, R. W., et al. 2011, ApJ, 732, 40
Draine, B. T., & Li, A. 2007, ApJ, 657, 810
Elitzur, M., & Shlosman, I. 2006, ApJL, 648, L101
Fanaroff, B. L., & Riley, J. M. 1974, MNRAS, 167, 31P
Farrah, D., Bernard-Salas, J., Spoon, H. W. W., et al. 2007, ApJ, 667, 149
Fazio, G. G., Hora, J. L., Allen, L. E., et al. 2004, ApJS, 154, 10
Fischera, J., Dopita, M. A., & Sutherland, R. S. 2003, ApJL, 599, L21
French, H. B., & Miller, J. S. 1980, PASP, 92, 753
Frogel, J. A., Persson, S. E., Matthews, K., & Aaronson, M. 1978, ApJ, 220, 75
Gallimore, J. F., Yzaguirre, A., Jakoboski, J., et al. 2010, ApJS, 187, 172
Genzel, R., & Cesarsky, C. J. 2000, ARA&A, 38, 761
González-Martín, O., Masegosa, J., Márquez, I., et al. 2015, A&A, 578, A74
Granato, G. L., & Danese, L. 1994, MNRAS, 268, 235
Granato, G. L., Danese, L., & Franceschini, A. 1997, ApJ, 486, 147
Gu, Q.-S., Huang, J.-S., Wilson, G., & Fazio, G. G. 2007, ApJL, 671, L105
Haas, M., Müller, S. A. H., Bertoldi, F., et al. 2004, A&A, 424, 531
Haas, M., Siebenmorgen, R., Schulz, B., Krügel, E., & Chini, R. 2005, A&A, 442, L39
Hardcastle, M. J., Alexander, P., Pooley, G. G., & Riley, J. M. 1996, MNRAS, 278, 273
Hardcastle, M. J., Evans, D. A., & Croston, J. H. 2009, MNRAS, 396, 1929
Heckman, T. M., Kauffmann, G., Brinchmann, J., et al. 2004, ApJ, 613, 109
Heesen, V., Croston, J. H., Harwood, J. J., Hardcastle, M. J., & Hota, A. 2014, MNRAS, 439, 1364
Ho, L. C., & Keto, E. 2007, ApJ, 658, 314
Hota, A., Rey, S.-C., Kang, Y., et al. 2012, MNRAS, 422, L38
Hu, J.-F., Cao, X.-W., Chen, L., & You, B. 2016, RAA, 16, 136
Jaffe, W., Ford, H. C., Ferrarese, L., van den Bosch, F., & O'Connell, R. W. 1993, Natur, 364, 213
Jensen, J. J., Hönig, S. F., Rakshit, S., et al. 2017, MNRAS, 470, 3071
Kennicutt, R. C. J. 1998, ARA&A, 36, 189
Kessler, M. F., Steinz, J. A., Anderegg, M. E., et al. 1996, A&A, 500, 493
Kharb, P., O'Dea, C. P., Tilak, A., et al. 2012, ApJ, 754, 1
Kharb, P., & Shastri, P. 2004, A&A, 425, 825
Kleijn, G. A. V., Baum, S. A., de Zeeuw, P. T., & O'Dea, C. P. 2002, AJ, 123, 1334
Kolokythas, K., O'Sullivan, E., Giacintucci, S., et al. 2015, MNRAS, 450, 1732
Laing, R. A., & Bridle, A. H. 1987, MNRAS, 228, 557
Laing, R. A., Bridle, A. H., Cotton, W. D., Worrall, D. M., & Birkinshaw, M. 2008, in ASP Conf. Ser. 386, Jet Spectra in FRI Radio Galaxies: Implications for Particle Acceleration, ed. T. A. Rector & D. S. De Young (San Francisco, CA: ASP), 110
Laing, R. A., Riley, J. M., & Longair, M. S. 1983, MNRAS, 204, 151
Lanz, L., Bliss, A., Kraft, R. P., et al. 2011, ApJ, 731, 52

Lebouteiller, V., Barry, D. J., Spoon, H. W. W., et al. 2011, ApJS, 196, 8
Leipski, C., Antonucci, R., Ogle, P., & Whysong, D. 2009, ApJ, 701, 891
Lilly, S. J., Longair, M. S., & Miller, L. 1985, MNRAS, 214, 109
Mack, K. H., Klein, U., O'Dea, C. P., & Willis, A. G. 1997, A&AS, 123, 423
Makovoz, D., & Marleau, F. R. 2005, PASP, 117, 1113
Marton, G., Schulz, B., Altieri, B., et al. 2016, in IAU Symp. 315, From Interstellar Clouds to Star-Forming Galaxies: Universal Processes?, ed. P. Jablonka, P. André, & F. van der Tak, E53 doi:10.1017/S1743921316008152
Merritt, D., & Ferrarese, L. 2001, ApJ, 547, 140
Metropolis, N., Rosenbluth, A. W., Rosenbluth, M. N., Teller, A. H., & Teller, E. 1953, JChPh, 21, 1087
Mor, R., Netzer, H., & Elitzur, M. 2009, ApJ, 705, 298
Morganti, R., Fanti, C., Fanti, R., Parma, P., & de Ruiter, H. R. 1987, A&A, 183, 203
Narayan, R., Mahadevan, R., & Quataert, E. 1998, in Theory of Black Hole Accretion Disks, ed. M. A. Abramowicz, G. Björnsson, & J. E. Pringle (Cambridge: Cambridge Univ. Press), 148
Nenkova, M., Ivezić, Ž, & Elitzur, M. 2002, ApJL, 570, L9
Nenkova, M., Ivezic, Z., & Elitzur, M. 1999, in LPI Contributions, Vol. 969, Thermal Emission Spectroscopy and Analysis of Dust, Disks, and Regoliths, ed. A. Sprague, D. K. Lynch, & M. Sitko (Houston, TX: LPI), 20
Nenkova, M., Sirocky, M. M., Ivezić, Ž, & Elitzur, M. 2008a, ApJ, 685, 147
Nenkova, M., Sirocky, M. M., Nikutta, R., Ivezić, Ž, & Elitzur, M. 2008b, ApJ, 685, 160
Nilson, P. 1973, Uppsala General Catalogue of Galaxies (Uppsala: Astronomiska Observatorium)
Noel-Storr, J., Baum, S. A., & O'Dea, C. P. 2007, ApJ, 663, 71
Noel-Storr, J., Baum, S. A., Verdoes Kleijn, G., et al. 2003, ApJS, 148, 419
Orr, M. J. L., & Browne, I. W. A. 1982, MNRAS, 200, 1067
Owen, F. N., Eilek, J. A., & Kassim, N. E. 2000, ApJ, 543, 611
Padovani, P., Alexander, D. M., Assef, R. J., et al. 2017, A&ARv, 25, 2
Perlman, E. S., Biretta, J. A., Sparks, W. B., Macchetto, F. D., & Leahy, J. 2001, ApJ, 551, 206
Perlman, E. S., Mason, R. E., Packham, C., et al. 2007, ApJ, 663, 808
Pier, E. A., & Krolik, J. H. 1992, ApJ, 401, 99
Pier, E. A., & Krolik, J. H. 1993, ApJ, 418, 673
Richings, A. J., Uttley, P., & Körding, E. 2011, MNRAS, 415, 2158
Roussel, H., Sauvage, M., Vigroux, L., & Bosma, A. 2001, A&A, 372, 427
Rowan-Robinson, M. 1995, MNRAS, 272, 737
Sales, D. A., Robinson, A., Axon, D. J., et al. 2015, ApJ, 799, 25
Schartmann, M., Meisenheimer, K., Camenzind, M., Wolf, S., & Henning, T. 2005, A&A, 437, 861
Schwarz, G. 1978, AnSta, 6, 461
Shi, Y., Rieke, G. H., Hines, D. C., Gordon, K. D., & Egami, E. 2007, ApJ, 655, 781
Sikora, M., Stasińska, G., Kozieł-Wierzbowska, D., Madejski, G. M., & Asari, N. V. 2013, ApJ, 765, 62
Silva, L., Granato, G. L., Bressan, A., & Danese, L. 1998, ApJ, 509, 103
Sirocky, M. M., Levenson, N. A., Elitzur, M., Spoon, H. W. W., & Armus, L. 2008, ApJ, 678, 729
Skrutskie, M. F., Cutri, R. M., Stiening, R., et al. 2006, AJ, 131, 1163
Smith, J. D. T., Draine, B. T., Dale, D. A., et al. 2007, ApJ, 656, 770
Spinoglio, L., & Malkan, M. A. 1992, ApJ, 399, 504
Storn, R., & Price, K. 1997, Journal of Global Optimization, 11, 341
Tadhunter, C. 2016, A&ARv, 24, 10
Tansley, D., Birkinshaw, M., Hardcastle, M. J., & Worrall, D. M. 2000, MNRAS, 317, 623
Temi, P., Brighenti, F., & Mathews, W. G. 2009, ApJ, 707, 890
Teplitz, H. I., Capak, P., Hanish, D., et al. 2012, AAS Meeting, 219, 428.06
ter Braak, C. J. F., & Vrugt, J. A. 2008, Statistics and Computing, 18, 435
Torrealba, J., Chavushyan, V., Cruz-González, I., et al. 2012, RMxAA, 48, 9
van der Wolk, G., Barthel, P. D., Peletier, R. F., & Pel, J. W. 2010, A&A, 511, A64
Verdoes Kleijn, G. A., Baum, S. A., de Zeeuw, P. T., & O'Dea, C. P. 1999, AJ, 118, 2592
Verdoes Kleijn, G. A., & de Zeeuw, P. T. 2005, A&A, 435, 43
Werner, M. W., Roellig, T. L., Low, F. J., et al. 2004, ApJS, 154, 1
Whysong, D., & Antonucci, R. 2004, ApJ, 602, 116
Willett, K. W., Stocke, J. T., Darling, J., & Perlman, E. S. 2010, ApJ, 713, 1393
Wu, Q., & Cao, X. 2006, PASP, 118, 1098
Xu, C., Livio, M., & Baum, S. 1999, AJ, 118, 1169
Zirbel, E. L., & Baum, S. A. 1995, ApJ, 448, 521